

Linear Neural Networks applied to Power Converters and AC Electrical Drives

M. Cirrincione(*), G. Cirrincione(°), M.Pucci(#), G.Vitale(#).

(*) University of Technology of Belfort-Montbéliard (UTBM), Belfort, France

(°) University of Picardie Jules Verne (UPJV), Amiens, France

(#) Institute of Intelligent Systems for Automation of the Italian National Research Council (ISSIA-CNR),
Palermo, Italy

Abstract: This contribution wants to show some recent applications of neural networks in the field of power electronics, with particular emphasis on the sensorless control of AC drives and examines improvements that can be attained when using linear neural networks. At first it presents some theoretical aspects of linear neural networks, particularly the TLS EXIN neuron. Then it describes some original applications in electrical drives and power quality as follows: 1) least square and neural identification of electrical machines 2) neural sensorless control of AC drives 3)neural enhanced single-phase DG system with APF capability Simulation and experimental results are provided to validate the theories.

1.Introduction

Artificial Intelligence (AI) has been recognized as an important tool in many fields among which Power Electronics (PE) and Electrical drives (ED). Many papers and books have been published and good surveys can be found in [1]-[10]. Recent advances make it possible to achieve higher performance and lower cost in a wide range of industrial, commercial, military, utility, and residential applications. In addition, AI can help more efficient use of electricity resulting in environmental protection. Nowadays these AI-applications range from modern power semiconductor devices, converter circuits, and electrical machine design to high-performance control of induction and synchronous motor drives, energy saving control, estimation, identification, sensorless control of drives, as well as to active harmonic filters and their principles and applications in the energy conversion for distributed generation. Another power application is their use in the diagnosis for detecting fault and pre-fault situations in electrical machines and drives and in power electronics complex systems.

In general the term AI should be interpreted, as for its applications in power electronics and drives, as Computational Intelligence [2], based on Soft-Computing (SC), which comprises several methodologies for the design and utilization of information and intelligent systems. SC is generally made up of Fuzzy Logic Systems (FLS), the Artificial Neural Networks (ANN) the Genetic Algorithms (GA) and the hybrid systems, in particular the neuro-fuzzy (fuzzy-neural), and the genetic assisted neural and fuzzy systems. All SC techniques have been conceived to suitably deal with the uncertainty of knowledge and data, typical of real-world applications. It is easy then to understand how the introduction of SC techniques has made it possible to boost power electronics and motor drive technology since the electrical

drive or power electronics application can evolve into an intelligent behaviour, meaning that it can embed some features of “learning”, “self-organizing” or “self-adapting. Particularly, the integration of SC can frequently lead up to a reduction of the development times and can avoid mathematical difficulties in system development, since SC techniques do not require the mathematical model of the system. With specific regard to automatic control aspects, for instance, the correct knowledge of the system (plant) model to be controlled is usually needed, and is typically expressed in terms of algebraic or differential equations, providing the system input-output relationship. These models can frequently be complex, rely on unrealistic assumptions and contain parameters that are measurable with difficulty, or can vary during the operation of the system. There are even cases in which the mathematical model of the system is not determinable at all. These problems could be overcome by adopting intelligent control techniques, which can be implemented even in absence of the plant mathematical model and can be significantly less sensitive versus parameter variations. While FLSs are rule-based techniques, aimed at reproducing the behaviour of the human brain, ANNs tend to reproduce its biological architecture. A different approach is that of GAs, or evolutionary computation, which are based on the principles of genetics (fittest theory of the evolution). GAs solve a problem of optimization on the basis of an evolutionary process providing the best (fittest) solution (survivor). Among the different SC techniques, ANNs seem to have maximum impact on power electronics and electrical drives [6]-[11]. In general the supervised ANN are the most employed, above all the Multi-Layer-Perceptron or the Radial Basis Function ones for their capacity to approximate any continuous functions and a huge literature exists (see cited bibliography above). However another kind of neuron can be applied, that is the linear neuron, or the so-called ADALINE (Adaptive Linear Neuron) [12], which, simple as it can appear, gives surprisingly good results.

This paper wants to introduce the basics of linear neural networks and explain the theoretical framework in which they are positioned. Particularly the linear neuron TLS EXIN [13] will be introduced, which has proved fitter than the usual least-squares methods for solving challenging problems when measurement errors and noise are present. In the end some applications are described to prove the suitability of linear neural networks in power electronics for distributed generation (DG), in parameter estimation for AC induction machines and in sensorless control for high-performance electrical drives.

2.The linear neural network (the ADALINE) and the TLS EXIN neuron

With respect to the general neural network model, a linear neural network or ADALINE, in its simplest form, consists only of the adaptive linear combiner, and its output is only the result of this summation. No output activation function is present, or, if preferred, the output function is the identity function. Fig. 1 shows this simple general ADALINE model:

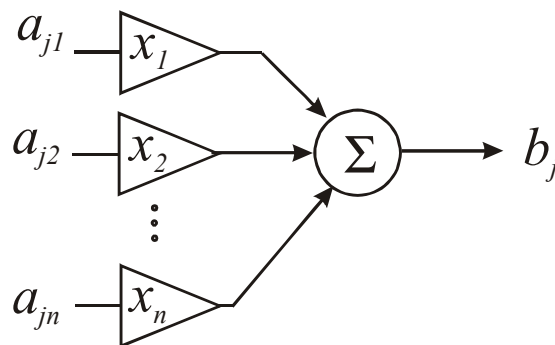


Fig.1: general form of an ADALINE or linear neural network

The output b_j can then be described by:

$$b_j = \sum_{i=1}^n a_{ji} x_i = \mathbf{a}_j^T \mathbf{x} \quad (1a)$$

where a_{ji} is the i -th component of the \mathbf{a}_j vector given as input at the j -th instant of time, x_i is the i -th component of the \mathbf{x} weight vector, b_j is the corresponding output at the j -th instant of time. If the vector $\mathbf{b} = [b_1 \dots b_j \dots b_m]^T \in \mathfrak{R}^m$ is considered as well as the matrix $A \in \mathfrak{R}^{m \times n}$ composed of m row vectors \mathbf{a}_j^T , then finding the weight vector \mathbf{x} (*the problem of linear parameter estimation*) is generally equivalent to solving the following overdetermined set of linear equations, on the basis of the training set (TS) made up of the expanded matrix $[A; \mathbf{b}]$:

$$A\mathbf{x} \approx \mathbf{b} \quad (1b)$$

In general $A \in \mathfrak{R}^{m \times n}$ is called *data matrix* and $\mathbf{b} \in \mathfrak{R}^m$ is called *observation vector*. Eq. (1b) is solved for by Least-Squares (LS) techniques. According to the classical OLS (Ordinary Least Squares) approach, errors are implicitly assumed to be confined to the observation vector. This assumption is however unrealistic. Actually also the data matrix is affected by noise, like sampling errors, human errors, modeling errors, measurement errors. In [14] and [15] some methods are presented to estimate the influence of these errors on the OLS solution. The TLS (Total Least Squares) method is a technique devised to make up for these errors. The TLS problem has been presented for the first time in [16], where it is solved by using the Singular Value Decomposition (SVD), as proposed in [15] and more completely in [17]. This estimation method stems historically from statistics literature, where it is called with the name of orthogonal regression or EIV (Errors-In-Variables) regression¹. A complete analysis of the TLS problem can be found in [13], where the algorithm of [16] is generalized to the non-generic case (non-generic TLS), where the initial algorithm failed to find a solution. According to the DLS (Data Least Squares) approach errors are assumed to be confined only to the data matrix [18]. The DLS case is particularly suitable for certain deconvolution problems, like in system identification or channel equalization.

In the mono-dimensional case ($n=1$) the resolution of the LS problem consists in determining the angular coefficient x of the straight line of the equation $Ax=b$. The LS technique solves for this problem by calculating the value of x which minimises the sum of squares of the distances among the elements (A_i, b_i) , with $i=1, \dots, m$, and the line itself. Fig. 2 shows the difference among the OLS, TLS and DLS in the monodimensional case.

OLS minimises the sum of squares of the distances in the b direction (error only in the observation vector); the OLS technique in a recursive form is called RLS (Recursive Least-Squares). TLS minimises the sum of squares in the direction orthogonal to the line (for this reason TLS is also called orthogonal regression) while DLS minimises the sum of squares in the A direction (errors only in the data matrix). In particular it must be expected that, in absence of noise, the results obtained with TLS are equal to those obtained with OLS; however in presence of increasing noise the performance of TLS remains higher than that of OLS, as TLS is less sensitive to noise. For these reasons the TLS algorithm is particularly suitable for estimation processes in which data are affected by noise; this is certainly the case in real world scenarios in which errors in the data matrix can easily occur. For a good introduction about OLS, TLS, and DLS see also [19], and [20].

¹ In EIV models the true values of observed variables satisfy unknown but exact linear relationships

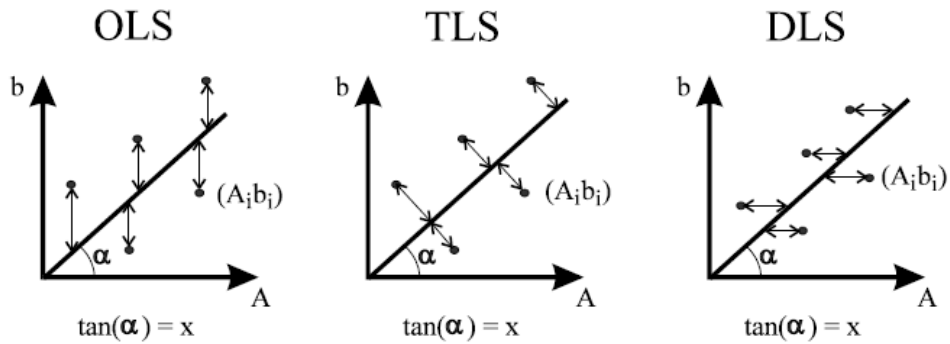


Fig.2: Differences between OLS, TLS, and DLS

In general the following three problems arise:

2.1 The OLS problem

The least-square solution is the one minimizing

$$\min_{\mathbf{b}' \in \mathcal{R}^m} \|\mathbf{b} - \mathbf{b}'\|_2 \quad \text{with the constraint } \mathbf{b}' \in R(A) \quad (2)$$

Where $R(A)$ is the column space of A . When a minimum of \mathbf{b}' is found, every vector satisfying

$$A\mathbf{x}' = \mathbf{b}' \quad (3)$$

is then called the OLS solution. It corresponds to the vector minimizing the following cost function

$$E_{OLS}(\mathbf{x}) = (A\mathbf{x} - \mathbf{b})^T (A\mathbf{x} - \mathbf{b}) \quad (4)$$

2.2 The DLS problem

The least-square solution is the one minimizing

$$\min_{A'' \in \mathcal{R}^{m \times n}} \|A - A''\|_F \quad \text{with the constraint } \mathbf{b} \in R(A'') \quad (5)$$

where $\|\cdot\|_F$ is the Frobenius norm. Once a minimum A'' is found, every \mathbf{x}'' satisfying

$$A''\mathbf{x}'' = \mathbf{b} \quad (6)$$

is called the DLS solution. In [13, p. 120] it is proved that it corresponds to the minimization of the cost function

$$E_{DLS}(\mathbf{x}) = \frac{(A\mathbf{x} - \mathbf{b})^T (A\mathbf{x} - \mathbf{b})}{\mathbf{x}^T \mathbf{x}} \quad (7)$$

2.3 The TLS problem and the TLS EXIN neuron

The least-square solution is the one minimizing

$$\min_{[\hat{A}; \hat{\mathbf{b}}] \in \mathfrak{R}^{m \times (n+1)}} \left\| [A; \mathbf{b}] - [\hat{A}; \hat{\mathbf{b}}] \right\|_F \quad \text{with the constraint } \hat{\mathbf{b}} \in R(\hat{A}) \quad (8)$$

When a minimum of $[\hat{A}; \hat{\mathbf{b}}]$ is found, every $\hat{\mathbf{x}}$ satisfying

$$\hat{A}\hat{\mathbf{x}} = \hat{\mathbf{b}} \quad (9)$$

is called TLS solution. It minimizes the sum of orthogonal squared distances (weighted residues squared sum):

$$E_{TLS}(\mathbf{x}) = \frac{(A\mathbf{x} - \mathbf{b})^T (A\mathbf{x} - \mathbf{b})}{1 + \mathbf{x}^T \mathbf{x}} = \frac{\left\| [A; \mathbf{b}] \begin{bmatrix} \mathbf{x}^T \\ -1 \end{bmatrix} \right\|_2^2}{\left\| \begin{bmatrix} \mathbf{x}^T \\ -1 \end{bmatrix} \right\|_2^2} \quad (10)$$

which corresponds to the Raleigh Quotient of $[A; \mathbf{b}]^T [A; \mathbf{b}]$

$$E_{MCA}(x) = \frac{\mathbf{u}^T [A; \mathbf{b}]^T [A; \mathbf{b}] \mathbf{u}}{\mathbf{u}^T \mathbf{u}} \quad (11)$$

with the constraint $u_{n+1} = -1$ (u_{n+1} is the last component of the vector u), which represents a hyperplane in the space u , called *TLS hyperplane*. Eq (11) shows that the solution can be found by using the Minor Component Analysis (MCA) [13], followed by a normalization of the result. It can be proven that the TLS solution is parallel to the right singular vector $\in \mathfrak{R}^{n+1}$ corresponding to the smallest singular value of $[A; \mathbf{b}]$ or equivalently to the smallest eigenvalue of $[A; \mathbf{b}]^T [A; \mathbf{b}]$. This results in the *TLS EXIN neuron learning law*:

$$x(t+1) = x(t) - \alpha(t)\gamma(t)\mathbf{a}_i + [\alpha(t)\gamma^2(t)]x(t) \quad (12)$$

with $[\mathbf{a}_i^T; b_i]^T$ i being the index, the i -th $[A; \mathbf{b}]$ row presented as input to the neuron at the time t , $\alpha(t)$ the learning factor (a positive scalar value decreasing with time)and,

$$\gamma(t) = \frac{\delta(t)}{1 + x(t)^T x(t)} \quad \delta(t) = x^T(t)\mathbf{a}_i - b_i \quad (13a,b)$$

The TLS EXIN neuron is a linear unit with n inputs (vector \mathbf{a}_i), n weights (vector \mathbf{x}), one output (scalar $y_i = \mathbf{x}^T \mathbf{a}_i$) and one training error (scalar $\delta(t)$). With this typology, the training is considered as *supervised*, being b_i the target. The quantity in brackets in (12) is positive, which implies that the second term in eq.(12) is a *reverse ridge regression*.

TLS EXIN can work either sequentially or in batch and block modes. Several methods for accelerating the TLS EXIN convergence speed have been implemented (in mode block and batch), as the Conjugate Gradient (CG) methods, the Scaled Conjugate Gradient (SCG) [21] has been employed or the Broyden-Fletcher-Goldfarb-Shanno (BFGS) algorithm [22] can be used, since Newton or quasi-Newton can be employed, since the nxn Hessian matrix of $E_{TLS}(\mathbf{x})$ is proven to be positive definite and therefore is not singular ([13][14]). The whole theory of this neuron, the convergence analysis can be found in [13]: **a significant result is**

that the origin belongs to the TLS domain of convergence. This means that if null initial conditions are chosen for (12) it always converges. In [13] OLS, TLS, and DLS problems are then encompassed in a general theoretical framework leading to the Generalized TLS EXIN neuron (GeTLS EXIN).

3. Least-Squares and Neural Identification of Induction Motors

3.1 Introduction to neural identification

The on-line estimation of the electrical parameters of an induction motor, either supplied by the power grid or in variable speed electric drive, is often crucial: e.g. for motors directly supplied by the power grid, subject to frequent start-ups and braking phases, the stator and rotor resistance estimation gives useful information about the variations of the temperature of windings, which is useful for deciding whether and when the subsequent start-up should take place in security conditions for avoiding potential damages in the machine. Or, as for induction motor variable speed drives, the correct on-line parameter estimation of the electrical parameters of the induction motor significantly affects the performance and the stability of the control system (as in rotor-flux-linkage oriented control or in direct torque control). Actually the electrical parameters of the machine, in rated working conditions, are usually measured with off-line methodologies at stand-still (no-load and locked-rotor tests) but in normal working conditions, however, these parameters can vary. Particularly, the values of the stator and rotor resistances vary because of the heating or cooling of the machine, while the stator and rotor inductances as well as the leakage coefficients can vary with the magnetization level of the machine core (saturation of the main flux). However, while the variation of the resistances is quite slow, since it is governed by the thermal time constants of the machine, the variation of the magnetic parameters is very fast; moreover the magnetic parameters vary whenever the machine works at speeds higher than the rated one, since in these working condition the magnetic flux is reduced (field-weakening) with consequent variation of all of the magnetic parameters. The rotor time constant can thus vary because of both the heating/cooling effects and the modification of the machine magnetization. In normal working conditions, the parameters could have percent variations even as much as 50% [24]-[27]. Thus if the parameters of the machine vary while the corresponding values assigned to the flux models used to control the drives are kept constant, the so-called “detuning” of the flux models occurs with resulting worse performance.

3.2 Problem formulation

The employment of any LS technique for real-time identification of induction machines requires the mathematical model of the machine itself to be rearranged. It is well-known that the induction motor model can be described by the following stator and rotor space-vector voltage equations in a general reference frame, which rotates at a general ω_g (in electrical angles per second):

$$\begin{aligned}
 \mathbf{u}_s^g &= R_s \mathbf{i}_s^g + \frac{d\boldsymbol{\psi}_s^g}{dt} + j\omega_g \boldsymbol{\psi}_s^g \\
 \mathbf{u}_r^g &= R_r \mathbf{i}_r^g + \frac{d\boldsymbol{\psi}_r^g}{dt} + j(\omega_g - \omega_r) \boldsymbol{\psi}_r^g \\
 \boldsymbol{\psi}_s^g &= L_s \mathbf{i}_s^g + L_m \mathbf{i}_r^g \\
 \boldsymbol{\psi}_r^g &= L_r \mathbf{i}_r^g + L_m \mathbf{i}_s^g
 \end{aligned} \tag{14}$$

If it is assumed that $d\omega_r/dt \approx 0$ (i.e. at standstill, slowly varying or constant speed) then eq.(14) can be written in a matrix form linear with the parameters, as follows:

$$\begin{pmatrix} \frac{di_{sx}^g}{dt} & i_{sx}^g & -(\omega_g - \omega_r)i_{sy}^g & -\omega_g i_{sy}^g & -\left(\frac{du_{sx}^g}{dt} - (\omega_g - \omega_r)u_{sy}^g\right) & -u_{sx}^g \\ \frac{di_{sy}^g}{dt} & i_{sy}^g & (\omega_g - \omega_r)i_{sx}^g & \omega_g i_{sx}^g & -\left(\frac{du_{sy}^g}{dt} + (\omega_g - \omega_r)u_{sx}^g\right) & -u_{sy}^g \end{pmatrix} \begin{pmatrix} K_1 \\ K_2 \\ K_{31} \\ K_{32} \\ K_4 \\ K_5 \end{pmatrix} \approx \begin{pmatrix} -\frac{d^2 i_{sx}^g}{dt^2} + (2\omega_g - \omega_r)\frac{di_{sy}^g}{dt} + \omega_g(\omega_g - \omega_r)i_{sx}^g \\ -\frac{d^2 i_{sy}^g}{dt^2} - (2\omega_g - \omega_r)\frac{di_{sx}^g}{dt} + \omega_g(\omega_g - \omega_r)i_{sy}^g \end{pmatrix} \quad (15)$$

Where the following K-parameters are introduced:

$$K_1 = \frac{1}{\sigma T_s} + \frac{\beta_0}{\sigma}, K_2 = \frac{\beta_0}{\sigma T_s}, K_{31} = \frac{1}{\sigma T_s}, K_{32} = \frac{\beta_0}{\sigma}, K_4 = \frac{1}{\sigma L_s}, K_5 = \frac{\beta_0}{\sigma L_s} \quad (16 \text{ a,b,c,d,e,f})$$

This matrix equation can be solved for by using the different Least-Squares methods presented in the previous section, in particular the OLS and the TLS methods. In particular the assumption $d\omega_r/dt \approx 0$ makes the observation vector affected directly by the approximation error, but, due to the presence of derivatives, which are sensitive to noise, also the data matrix is affected by error. So, in dependence on how much the errors in the data matrix and the observation vector affect the matrix equation (15), either the OLS or the TLS method should be used. In any case it is apparent from the matrix equation (15) that the two scalar equations that make it up are linearly independent. This means that in transient conditions or in non-sinusoidal steady state the data matrix is full rank and the LS solution can be obtained. However in sinusoidal steady state the data matrix has rank 2 and thus only two parameters can be computed. This means that the estimation of all the parameters cannot be made in steady state. However only 4 independent parameters can be retrieved from the K-parameters, that is i.e. : $R_s, R_r, \sigma, \beta_0 = 1/T_r$ as follows:

$$T_r = \frac{K_4}{K_5}, \sigma = \frac{K_5}{K_4 K_{32}} = \frac{K_5}{K_4(K_1 - K_{31})}, L_s = \frac{K_{32}}{K_5} = \frac{K_1 - K_{31}}{K_5}, R_s = \frac{K_2}{K_5} = \frac{K_{31}}{K_4} = \frac{K_1 K_5 - K_{32}}{K_4 K_5} \quad (17 \text{ a, b, c, d})$$

As recalled in [28], L_m, L_r, R_r cannot be obtained independently as rotor flux-linkages are unknown: thus machines with identical rotor time constant and identical ratio L_m^2/L_r have the same input/output (voltage/current) equations.

3.3 Implementation issues

Remark that for the implementation of the LS technique it is necessary to use both analog and digital filters. The estimation algorithm needs the signals of the stator voltages and currents, their derivatives, up to the second order for the current and the first order for the voltage, and the machine speed. Since the motor can be supplied both by the electric grid and by a VSI inverter, low-pass analog filters for stator voltage and current signals are needed to avoid aliasing phenomena. The presence of filters, however, causes distortion and time delays of the processed signals which, therefore, at each time instant, should be synchronized with one another in order to respect the dynamic equation of the induction machine. Fig. 3 shows the complete scheme used for processing all the signals needed by the identification algorithm. It is composed of [29][30]:

- Four analog low pass anti-aliasing filters (B(s) block in Fig. 3) which filter the stator voltage and current signals from the voltage and current sensors in the drive.

- Four digital low pass filters ($F(z)$ block in Fig. 3) reducing high order harmonics and the noise of the stator voltage and current signals which can be amplified by the following differentiator filters.
- Six digital differentiator filters ($D(z)$ block in Fig. 3) which allow to obtain the derivatives of the stator voltages (up to the first order) and currents (up to the second order) of the drive.

Since, in the application under study, the analog-to-digital converter of the voltage and current signals has a sampling time $T_s=100 \mu s$ (sampling frequency $f_s=10 \text{ kHz}$), it is necessary to cut off all harmonics of these signals from 5 kHz upwards to avoid aliasing phenomena. Bessel low-pass analog filters have been chosen for this task because they can be easily designed with an almost exactly linear phase characteristic.

Since the derivatives of voltage and current signals are necessary, digital FIR (Finite Impulse Response) differentiator filters (blocks $D(z)$ in Fig. 3) have been designed. FIR filters have been chosen for their characteristic to have an exactly linear phase diagram. These filters implement the transfer function $D(j\omega)=j\omega$ in the ω -domain. Finally digital low pass FIR filters have been chosen (blocks $F(z)$ in Fig. 3). Since all of the signals processed by the estimation algorithm must be synchronized, whenever a stator voltage or current signal is processed by the differentiator filter, the other signals, which are not differentiated and are used in the identification algorithm, must be delayed in time with the group delay of the differentiator filter. With reference to the experimental implementation of this methodology, an electronic card with 6 analog low-pass 4-th order Bessel filters has been built while all digital filters (low-pass FIR filters and differentiator FIR filters) along with the LS algorithm have been implemented by software on a DSP.

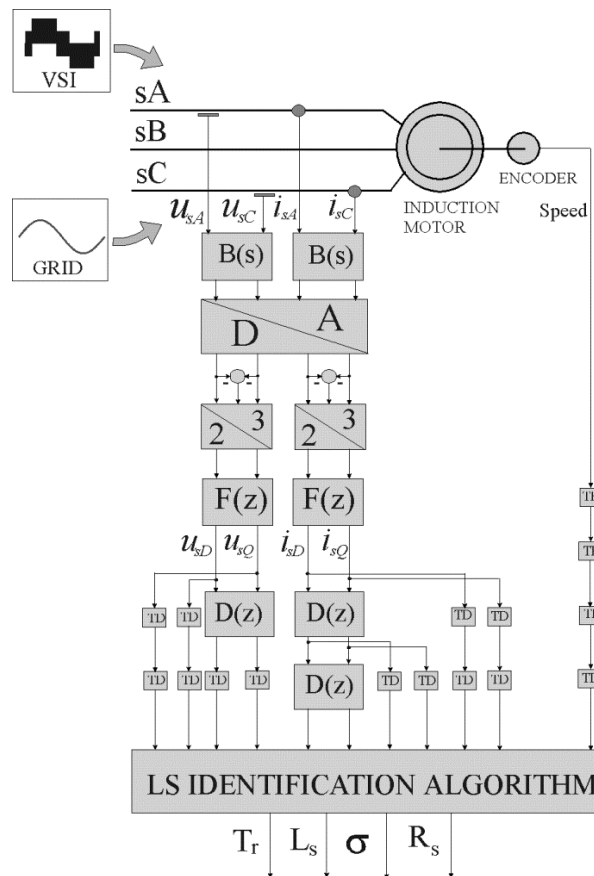


Fig. 3: Signal Processing System

3.4 Test set-up

The test set-up that has been built for the experimental verification of the parameter estimation algorithm consists of

- One three-phase induction motor with rated values shown in Table I;
- One electronic power converter (three-phase diode rectifier and VSI inverter composed of 3 IGBT modules without any control system) of rated power 7.5 kVA;
- One electronic card with voltage sensors (model LEM LV 25-P) and current sensors (model LEM LA 55-P) for monitoring the instantaneous values of the stator phase voltages and currents;
- One voltage sensor (Model LEM CV3-1000) for monitoring the instantaneous value of the DC link voltage;
- One electronic card with analog 4th order low-pass Bessel filters and cut-off frequency of 800 Hz;
- One incremental encoder (model RS 256-499, 2500 pulses per round);
- One DSPACE card (model DS1103) with a floating-point DSP;

The VSI inverter is driven by an asynchronous space-vector vector pulsewidth modulation (SV-PWM) technique (switching frequency $f_{PWM} = 5\text{kHz}$) implemented by software on the DSPACE card; the DC link voltage sensor permits taking into account the instantaneous value of the DC link voltage for the modulation. Fig. 4 shows the electric scheme of the adopted test set-up, while Fig. 5 shows its photograph.

Table I : Parameters of the induction motor

Rated power P_{rated} [kW]	2.2
Rated voltage U_{rated} [V]	220
Rated frequency f_{rated} [Hz]	50
Pole-pairs	2
Stator resistance R_s [Ω]	3.88
Stator inductance L_s [mH]	252
Rotor resistance R_r [Ω]	1.87
Rotor inductance L_r [mH]	252
3-phase magnetizing inductance L_m [mH]	236
Moment of inertia J [$\text{kg}\cdot\text{m}^2$]	0.0266

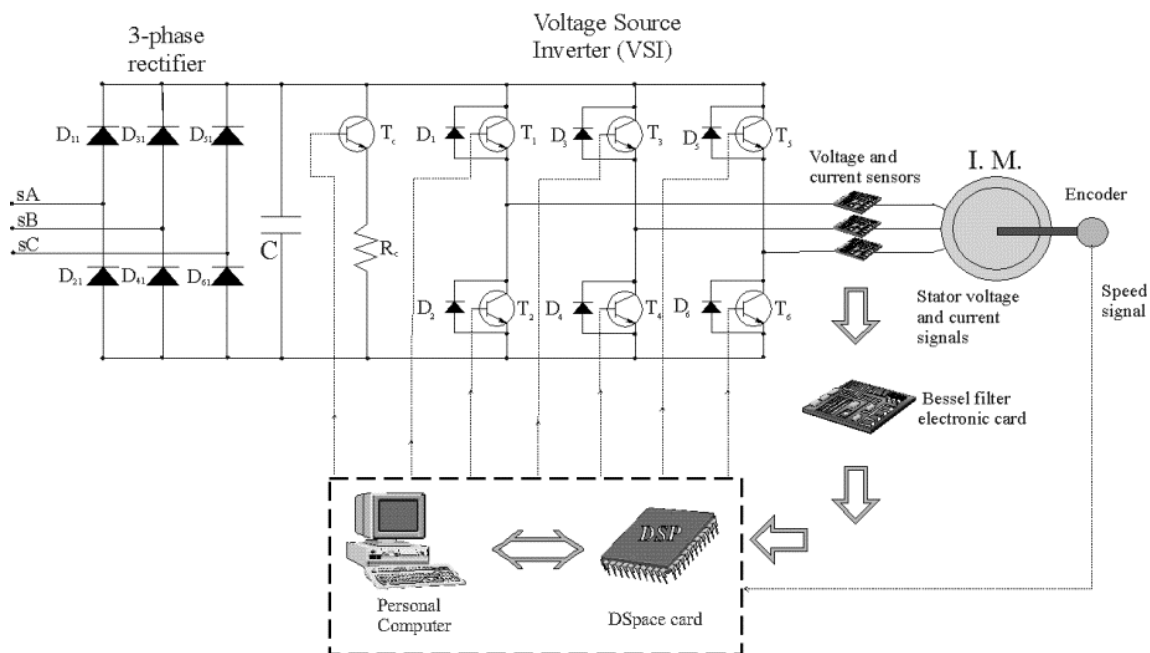


Fig.4: The electric scheme of the adopted test set-up



Fig. 5: Photograph of the experimental rig

3.5 Experimental results

The least-squares method has been verified numerically in simulations performed in Matlab® and Simulink® and applied experimentally on the test setup described above. The parameters of the induction motor used in the simulation are listed in Tab. I. In the experiments the motor has been supplied by an asynchronous SV-PWM driven VSI using a voltage/frequency open-loop control. The pulsewidth modulation as well as the open-loop scalar control algorithm have been implemented in software on the DSP of the dSPACE 1103 board employing the Matlab® - Simulink® - Real Time Workshop® - Real Time Interface® software. V-instruments have been employed for controlling/monitoring the drive and all the electrical and mechanical signals of the motor, e.g. the rotor speed, the DC link voltage and the stator voltages/currents. The LS algorithm has been implemented on the DSP board. In all tests the motor, both in simulation and experimentally, has been supplied by the VSI with sinusoidal reference voltage of 220 V at 50 Hz. Fig.6 shows, both in simulation and experimentally, the rotor speed, the i_{sA} stator current of the phase A and the stator current locus i_{sD} - i_{sQ} during up with no load.

The implementation of this method during these tests both in simulation and experimentally without noisy perturbations, are shown in Table II when using the OLS and the TLS methods. The initial values of the K-parameters have always been set to zero, to ensure convergence as explained at the end of §2. Table II shows the simulation and experimental results in terms of estimated steady-state parameters and percent estimation errors, obtained respectively with OLS and TLS. The reference values of the parameters have been measured with the usual locked rotor test. From table II it is apparent that the TLS solution is from a vector point of view closer to the true value than OLS. Therefore the estimation results are to be considered more accurate. Remark that in the experimental tests the true values of the parameters are those measured with the usual no-load and locked-rotor tests, which are retrieved under operating conditions which differ from those of the test: thus the machine parameters computed by the LS method can be slightly different from those obtained traditionally.

It is interesting to look at the error surfaces obtained with the two methods in fig. 7. The 3-D plots are drawn by varying just two K-parameters and letting the remaining ones be at values given by Table I. The flatness in the OLS error cost along the K_2 direction is due to the very small size of the singular value of \mathbf{A} corresponding to K_2 , which implies high 2-norm condition numbers [9] The computation of the other singular values shows that they are grouped together and this confirms that only K_2 is difficult to be estimated.

Table II
 estimated K-parameters (simulation and experimental results, OLS and TLS)

Simulation Results				
	OLS $\times 10^3$	TLS $\times 10^3$	OLS err. %	TLS err. %
K_1 [s^{-1}]	0.1886	0.1888	0.21	0.11
K_2 [s^{-2}]	1.267	0.9364	33.8	1.05
K_{s1} [s^{-1}]	0.1271	0.1280	0.37	0.34
K_4 [H^{-1}]	0.0328	0.0329	0.15	0.09
K_5 [$s^{-1} H^{-1}$]	0.2432	0.2413	0.29	1.06

Experimental Results				
	OLS $\times 10^3$	TLS $\times 10^3$	OLS err. %	TLS err. %
K_1 [s^{-1}]	0.1887	0.1794	0.14	5.09
K_2 [s^{-2}]	1.373	0.9480	45.11	0.16
K_{s1} [s^{-1}]	0.1229	0.1172	3.60	8.09
K_4 [H^{-1}]	0.0328	0.0324	0.16	1.53
K_5 [$s^{-1} H^{-1}$]	0.2580	0.2470	5.78	1.17

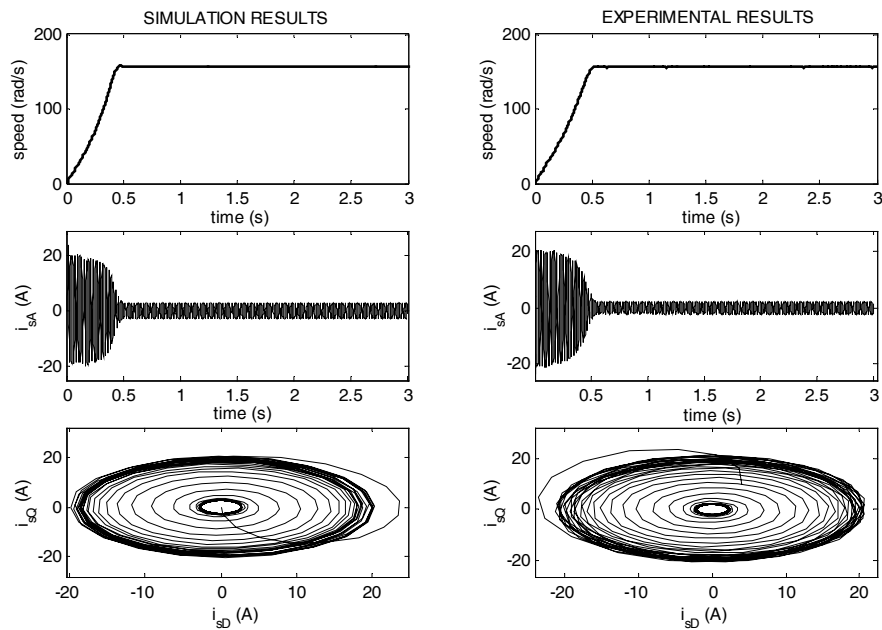


Fig. 6. Rotor speed, i_{sD} , i_{sQ} waveforms (simulation and experimental results)

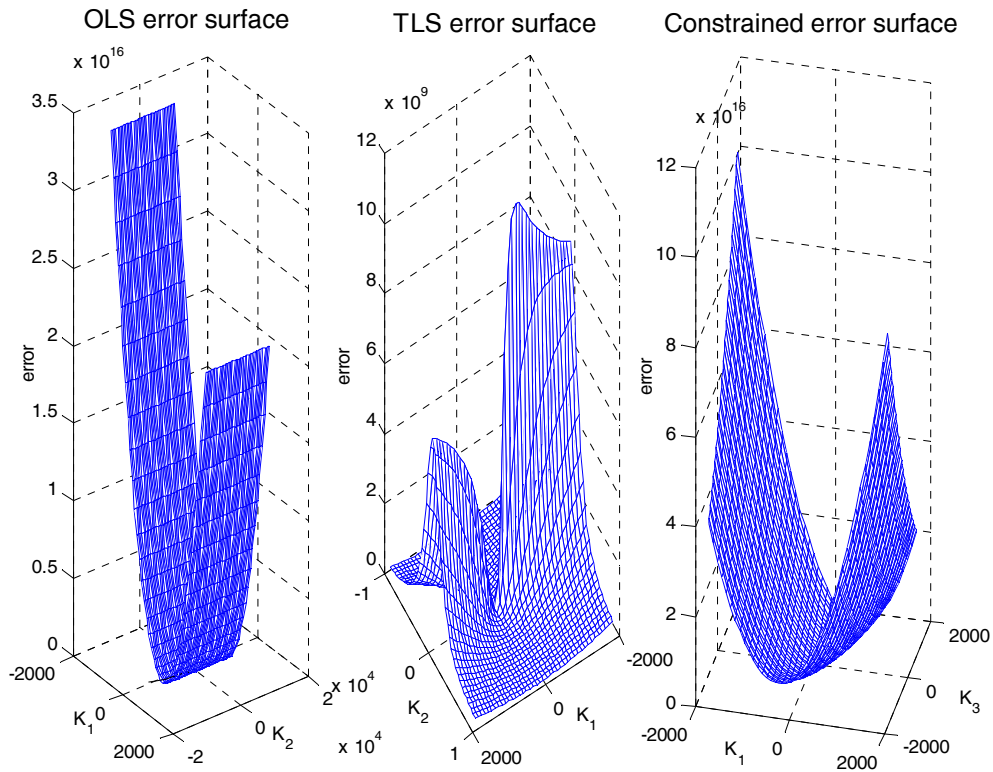


Fig. 7. 3-D error surfaces for OLS, TLS, and constrained OLS (from [9.100])

To check the robustness of TLS against noise, a uniformly distributed noise between -5% and $+5\%$ of the rated voltage and current has been given to each signal so as to have noisy elements both in the data matrix and in the observation vector. The electrical drive has been submitted to the same tests as described above but, to take into account the statistical effect of the random noise, each test has been repeated 50 times: in this way the statistical average of all the estimation has been computed. To speed convergence a BFGS method, which requires blocks of data, has been implemented on the DSP. The size of these blocks has been kept low not to overload the DSP.

Fig. 8 and Fig. 9 show the true parameters of the machine and the waveforms of the average parameter estimation, computed by the OLS and TLS, respectively in simulation and in the experimentation, when the signals are corrupted by the noise. The shift in time between the OLS and TLS curves is due to the different length of the block for each of them. The electrical parameters are updated every 0.3 s.

Tab. III shows the percentage error of the K-parameters at the end of the estimating process both with OLS and TLS as well as their global errors computed as the 2-norm, divided by the 2-norm of the true K-parameters vector, of the difference between the solution vector obtained with each method and the true K-parameters vector. These results show on the one hand that the OLS solution deteriorates in comparison with the TLS one in the presence of the noise, and on the other hand that the TLS solution goes away from the solution, especially in the estimation of K_2 ,

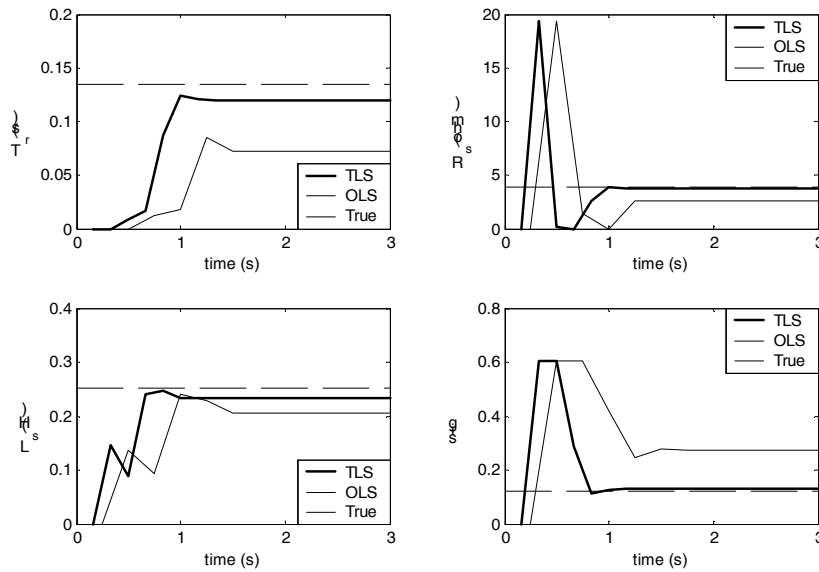


Fig. 8: Real and estimated electrical parameters of the motor with noise (simulation results)

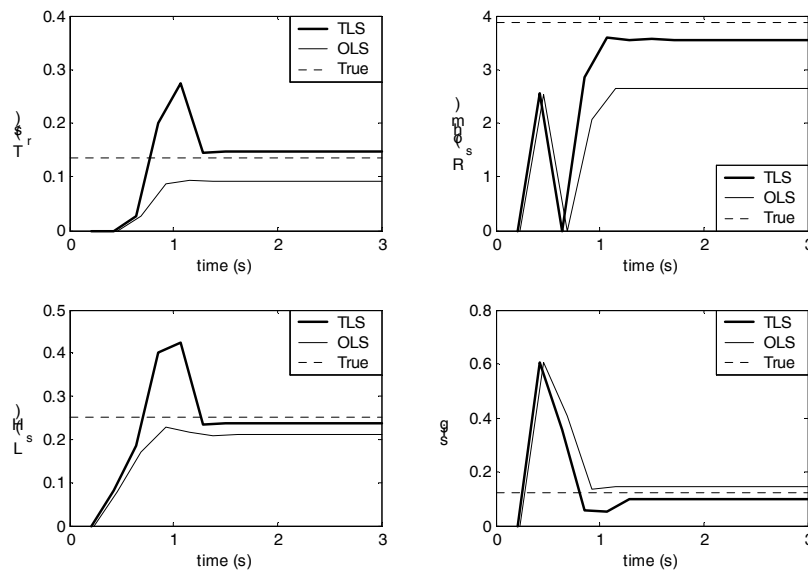


Fig. 9: Real and estimated electrical parameters of the motor with noise (experimental results)

3.6 Conclusions about neural parameter estimation

As for parameter estimation in AC motors, the advantage of using the TLS EXIN neuron is primarily the existence of a complete theory [13] which proves its convergence and accuracy as well as its tracking capability in slowly varying systems. For all these reasons, this technique suitable to be applied to induction motors, either supplied by the electrical grid or belonging a high performance electrical drive with any control system, and therefore with any supply condition.

As for its feasibility in industrial applications, this methodology presents in general the following advantages:

- it is simpler and less computationally cumbersome than the other algorithms in literature, like the Extended Kalman Filter , the Extended Luenberger Observer , the Model Reference Adaptive System;
- it does not use a frequency domain analysis or maximum likelihood for retrieving the electrical parameters;
- it allows the four electrical parameters to be estimated during a speed transient of the machine and one electrical parameter in sinusoidal steady-state;
- it can be applied with few modifications to the off-line identification of the machine at standstill during the self-commissioning of the drive;
- it does not require any a priori knowledge of the electrical parameters of the motor or its name-data;
- it can be applied both to FOC and DTC drive with slight modifications(useful in industrial applications as it reduces the development time);
- it permits computing the variation of the parameters due to different magnetic excitations (useful when the drive operates in the field weakening region).

4. Neural Sensorless Control of AC Drives (TLS EXIN Full-Order Luenberger Adaptive Observer)

4.1 Introduction

The neural sensorless control of AC drives is an enormous issue. Many neural based techniques have been used to retrieve the speed of induction motors, ranging from open-loop techniques [31] to MRAS (Model Reference Adaptive Systems) using the MLP trained with the Back-Propagation (BPN) algorithm [32]-[37] or sliding-mode neuro-fuzzy speed controller [38]. A classical off-line use of the MLP for speed computation has been adopted in [39]. However an up-to-date state of the art of neural sensorless control can be found in ch.11 of ref. [9]. Here another approach is described based on the structure of the Full-Order Luenberger Adaptive Observer [40][41]: the state equations of the induction motor are discretized and re-arranged to be used by a linear neural network (ADALINE) so that the TLS EXIN neuron can be used to train on-line the ADALINE and estimate the rotor speed.

4.2 Problem formulation

If the stator current and the rotor flux-linkage space-vectors are chosen as state variables, the state equations of the induction machine in the stationary reference frame can be written as:

$$\frac{d}{dt} \begin{bmatrix} \mathbf{i}_s \\ \boldsymbol{\Psi}'_r \end{bmatrix} = \frac{d\mathbf{x}}{dt} = \begin{bmatrix} \mathbf{A}_{11} & \mathbf{A}_{12} \\ \mathbf{A}_{21} & \mathbf{A}_{22} \end{bmatrix} \begin{bmatrix} \mathbf{i}_s \\ \boldsymbol{\Psi}'_r \end{bmatrix} + \begin{bmatrix} \mathbf{B}_1 \\ \mathbf{0} \end{bmatrix} \mathbf{u}_s = \mathbf{A} \mathbf{x} + \mathbf{B} \mathbf{u}_s \quad (18 \text{ a,b})$$

$$\mathbf{i}_s = \mathbf{C} \mathbf{x}$$

where:

$$\mathbf{A}_{11} = -\{R_s/(\sigma L_s) + (1-\sigma)/(\sigma T_r)\} \mathbf{I} = a_{11} \mathbf{I},$$

$$\begin{aligned}
\mathbf{A}_{12} &= L_m / (\sigma L_s L_r) \{ (1/T_r) \mathbf{I} - \omega_r \mathbf{J} \} = a_{12} \{ (1/T_r) \mathbf{I} - \omega_r \mathbf{J} \}, \\
\mathbf{A}_{21} &= \{ L_m / T_r \} \mathbf{I} = a_{21} \mathbf{I}, \\
\mathbf{A}_{22} &= - (1/T_r) \mathbf{I} + \omega_r \mathbf{J} = a_{22} \{ (1/T_r) \mathbf{I} - \omega_r \mathbf{J} \} \\
\mathbf{B}_1 &= 1 / (\sigma L_s) \mathbf{I} = b \mathbf{I}
\end{aligned} \tag{19 a,b,c,d,e}$$

with:

$$\mathbf{i}_s = [i_{sD} \quad i_{sQ}]^T, \quad \mathbf{u}_s = [u_{sD} \quad u_{sQ}]^T, \quad \Psi_r = [\Psi_{rd} \quad \Psi_{rq}]^T, \quad \mathbf{C}' = [\mathbf{0} \quad \mathbf{I}], \quad \mathbf{C} = [\mathbf{I} \quad \mathbf{0}], \quad \mathbf{I} = \begin{bmatrix} 1 & 0 \\ 0 & 1 \end{bmatrix}, \\
\mathbf{J} = \begin{bmatrix} 0 & -1 \\ 1 & 0 \end{bmatrix}.$$

In the above state representation $\mathbf{x} = [\mathbf{i}_s, \mathbf{y}_r']$ is the state vector, composed of the stator current and rotor flux linkage direct and quadrature components in the stationary reference frame, \mathbf{u}_s is the input vector composed of the stator voltage direct and quadrature components in the stationary reference frame, \mathbf{A} is the state matrix (4x4 matrix) depending on the rotor speed ω_r , \mathbf{B} is the input matrix and finally \mathbf{C} is the output matrix.

4.3 The adaptive speed observer

The full-order Luenberger state observer can be obtained from eq. (18), if a correction term is added containing the difference between the actual and estimated states. In particular, since the only measurable state variables are the stator currents, the correction term involves only the error vector on the stator current $\mathbf{e}_{rr} = (\mathbf{i}_s - \hat{\mathbf{i}}_s)$, as in the following:

$$\frac{d\hat{\mathbf{x}}}{dt} = \hat{\mathbf{A}}\mathbf{x} + \mathbf{B}\mathbf{u}_s + \mathbf{G}(\mathbf{i}_s - \hat{\mathbf{i}}_s) \tag{20}$$

where $\hat{}$ means the estimated values and \mathbf{G} is the observer gain matrix which is designed so that the above observer is stable. For the proper choice of the observer gain matrix see [40][41].

4.4 TLS-based Speed Estimation

The Total Least-Squares (TLS) based speed observer derives from a modification of (18), in the sense that it exploits the two first scalar equations to estimate the rotor speed, as shown below in discrete form for digital implementation [41].

The first two scalar equations of the matrix equation (18) can be written as:

$$\begin{cases} \frac{di_{sD}}{dt} = a_{11} i_{sD} + a_{12} p_r \hat{\Psi}_{rd} + a_{12} \hat{\omega}_r \hat{\Psi}_{rq} + b u_{sD} \\ \frac{di_{sQ}}{dt} = a_{11} i_{sQ} + a_{12} p_r \hat{\Psi}_{rq} - a_{12} \hat{\omega}_r \hat{\Psi}_{rd} + b u_{sQ} \end{cases} \tag{21}$$

where the current components are measured variables and the rotor flux and speed are estimated ones. Moving from the continuous domain to the discrete one, and approximating

the continuous derivative with the discrete filter $\frac{1-z^{-1}}{T_s z^{-1}}$, where T_s is the sampling time of the

control systems, the following equations can be deduced where k is the current time sample.

$$\begin{bmatrix} a_{12} T_s \hat{\Psi}_{rq}(k-1) \\ -a_{12} T_s \hat{\Psi}_{rd}(k-1) \end{bmatrix} \hat{\omega}_r(k-1) = \begin{bmatrix} i_{sD}(k) - i_{sD}(k-1) - a_{11} T_s i_{sD}(k-1) - a_{12} p_r T_s \hat{\Psi}_{rd}(k-1) - b T_s \hat{u}_{sD}(k-1) \\ i_{sQ}(k) - i_{sQ}(k-1) - a_{11} T_s i_{sQ}(k-1) - a_{12} p_r T_s \hat{\Psi}_{rq}(k-1) - b T_s \hat{u}_{sQ}(k-1) \end{bmatrix} \tag{22}$$

where $p_r=1/T_r$.

However also the four scalar equations in (18) can be exploited in order to retrieve the speed estimation, as shown below [40]:

$$\begin{bmatrix} a_{12}T_s\hat{\psi}_{rq}(k-1) \\ -a_{12}T_s\hat{\psi}_{rd}(k-1) \\ -a_{22}T_s\hat{\psi}_{rq}(k-1) \\ a_{22}T_s\hat{\psi}_{rd}(k-1) \end{bmatrix} \hat{\omega}_r(k-1) = \begin{bmatrix} i_{sD}(k) - i_{sD}(k-1) - a_{11}T_s i_{sD}(k-1) - a_{12}p_r T_s \hat{\psi}_{rd}(k-1) - bT_s \hat{u}_{sD}(k-1) \\ i_{sQ}(k) - i_{sQ}(k-1) - a_{11}T_s i_{sQ}(k-1) - a_{12}p_r T_s \hat{\psi}_{rq}(k-1) - bT_s \hat{u}_{sQ}(k-1) \\ -\hat{\psi}_{rd}(k) + \hat{\psi}_{rd}(k-1) + a_{21}T_s i_{sd}(k-1) + a_{22}T_s/T_r \hat{\psi}_{rd}(k-1) \\ -\hat{\psi}_{rq}(k) + \hat{\psi}_{rq}(k-1) + a_{21}T_s i_{sq}(k-1) + a_{22}T_s/T_r \hat{\psi}_{rq}(k-1) \end{bmatrix} \quad (23)$$

Both eq.s (22) and (23) are classical matrix equation of the type $\mathbf{Ax} \approx \mathbf{b}$, where \mathbf{x} is the unknown vector, equal to $\hat{\omega}_r$. Least-squares (LS) techniques can therefore be adopted to solve them in recursive form. The matrix \mathbf{A} is composed of the d-q axis components of the rotor flux linkage, which can be affected by errors and noise resulting measurements and the same can be said for the observation vector \mathbf{b} which is also composed of the d-q axis components of the rotor flux linkage and the d-q components of the stator current space vector; the problem under hand is therefore a TLS problem, rather than an OLS one.

Fig. 10 shows the block diagram of the TLS EXIN Full-Order Adaptive Observer.

It should be remarked that the computation of the rotor speed by means of the TLS estimator is performed through the minimization of the residual of the matrix equation (22) or (23). The residual is strongly dependant on the rotor flux estimation error, while all its other terms are dependent on the measured values of the electrical variables (i_s and u_s) and they are also affected by measurement errors. The TLS inherently gives the best solution for the rotor speed in spite of these uncertainties. From experimental results [9] it appears that (23) solution gives better results than (22), even if it is computationally more bulky. Actually this offers higher robustness to parameter uncertainty

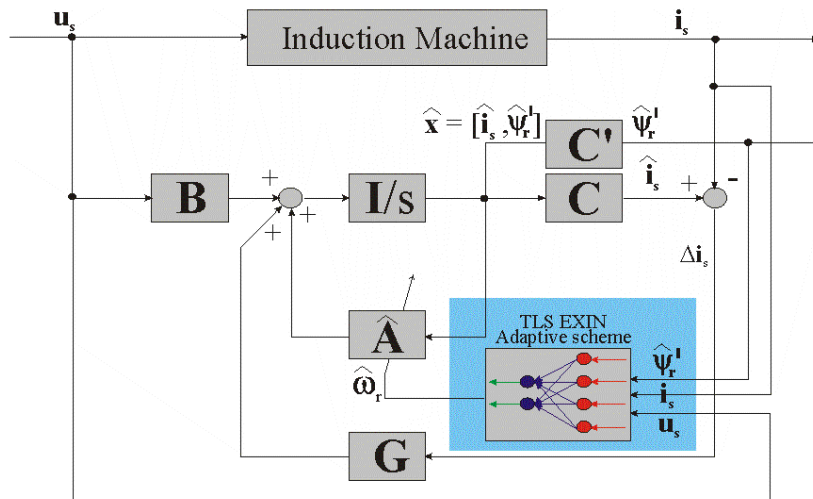


Fig. 10: Block diagram of the TLS EXIN Full-Order Adaptive Observer

4.5 Experimental results

The adopted test setup is the same described in section 3.4.

The TLS EXIN Full-Order Luenberger Adaptive Observer has been tested experimentally on a FOC induction motor drive.

The dynamic performance of the drive have been verified by giving the following set of speed step variations $0 \rightarrow 100 \rightarrow -100 \rightarrow 0$ rad/s at no-load. Fig. 11 shows the estimated, measured speed and the speed estimation error obtained with the TLS EXIN Full-Order Luenberger

Adaptive Observer and Fig. 12 shows the corresponding rotor flux linkage amplitude and electromagnetic torque. These figures show that the speed reversal with both the observers is accomplished in 0.29 s and the torque response is practically instantaneous. By employing the TLS based observer, the instantaneous speed estimation error is maximum during the first speed transient, when the adaptive observer is not yet correctly tuned due to the mismatch between the parameters of the observer and the real ones of the machine, while afterwards it is almost negligible also during the speed reversal. This is not the case of the classic adaptive observer, presenting an instantaneous speed estimation error during the speed reversal of almost as much as 20 rad/s.

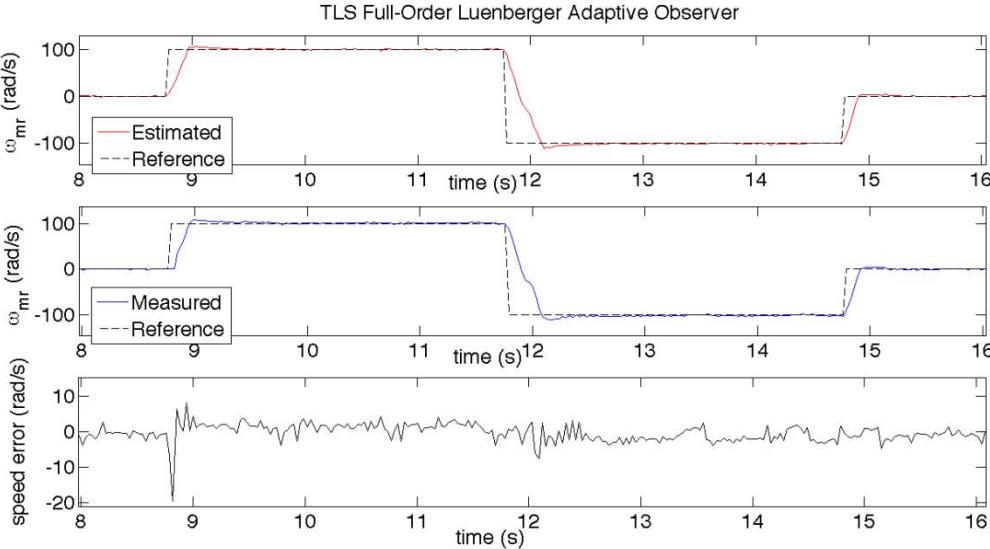


Fig. 11: reference, estimated, measured speed and speed estimation error during a set of speed steps with a reversal from 100 rad/s (955 rpm) to -100 rad/s with the TLS EXIN Full-Order Luenberger Adaptive Observer

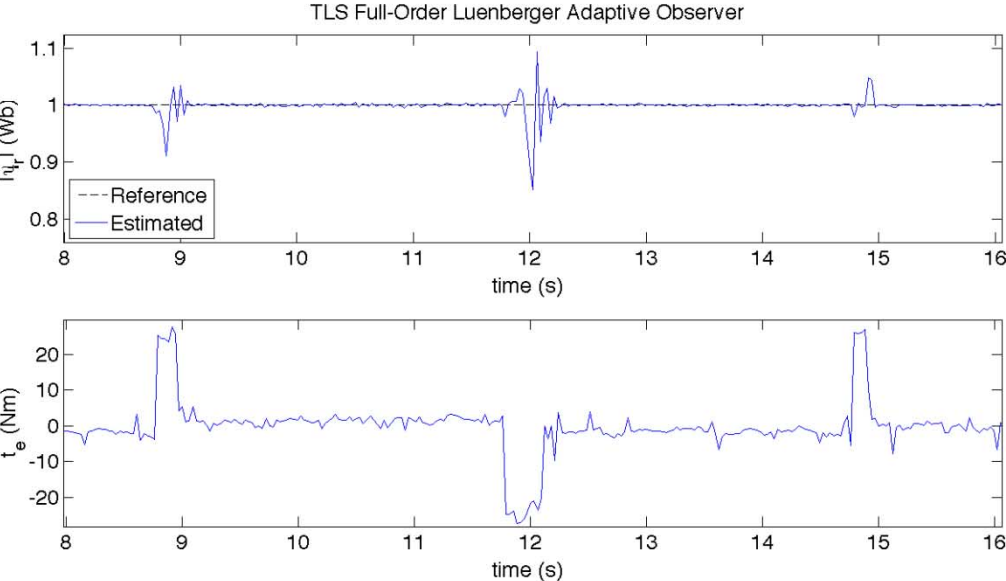


Fig. 12: rotor flux linkage amplitude and electromagnetic torque during a set of speed steps with a reversal from 100 rad/s (955 rpm) to -100 rad/s (-955 rpm) with the TLS EXIN Full-Order Luenberger Adaptive Observer

Finally, the dynamic performance of the proposed observer has been tested by giving it a square wave speed reference with the lowest possible amplitude and the highest possible pulsation. Fig. 13 shows the reference, measured and estimated speed obtained giving the drive a square speed waveform reference of amplitude 2 rad/s and pulsation 0.3 rad/s. It shows the capability of the observer to follow a square waveform reference of very low amplitude and high frequency. It should be noted that, during the zero crossing of the speed, there is a time interval during which the real speed of the machine remains equal to zero.

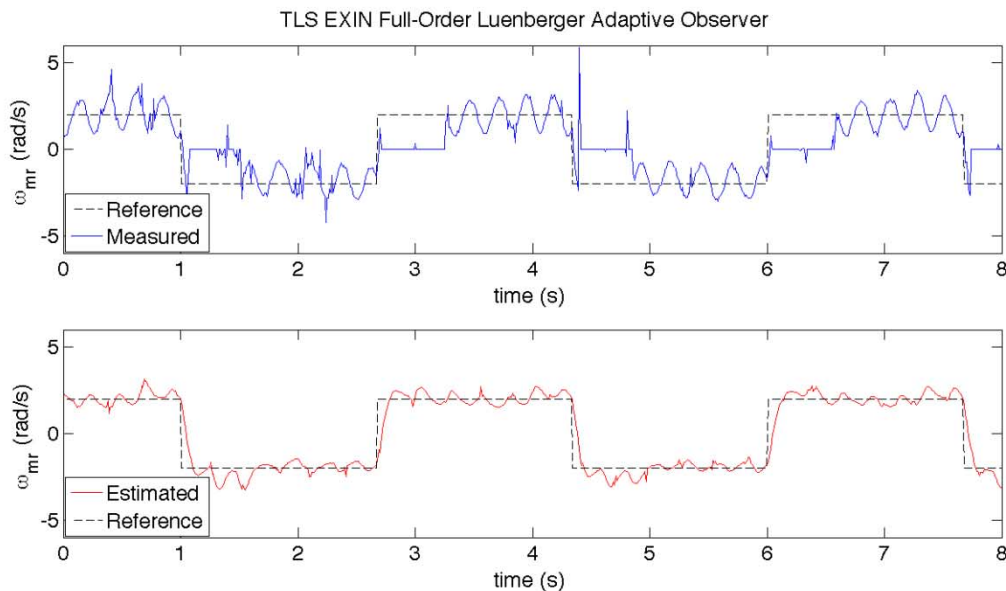


Fig. 13: reference, measured and estimated speed in a square wave reference of amplitude 2 rad/s and pulsation 0.3 rad/s with the TLS EXIN Full-Order Luenberger Adaptive Observer (from [9]).

The drive has been then operated at the rated rotor flux-linkage at zero speed. The test has been performed at no-load and at the load of 5 Nm (about 50% of the rated load). Figs 14, 15 show the waveforms of the reference, measured, estimated speed and speed estimation error for a time interval of 60 s, obtained respectively with the TLS and the classic full-order observers. They show that with the TLS observer, after the magnetisation of the machine, the drive can work properly at zero speed and at no-load, even without any signal injection.

This is mainly due to the fact that the TLS algorithm estimating the rotor speed uses the measured stator current signals and not the estimated ones, as in the classic observer. In particular the estimated speed has slight oscillations around 0 rad/s and the measured speed is always zero. In contrast to this, the classic observer at almost 15 s after the magnetisation of the machine has an unstable behaviour with the machine running at 45 rad/s with a mean speed estimation error of 13.74 rad/s. The drive has exhibited this kind of unstable behaviour after repeating such tests more times. Figs 16 shows a comparison among several speed observer in a speed reversal from 100 rad/s to -100 rad/s and highlight the best behaviour among all of the TLS full order observer which presents the minimum transient estimation error. Fig 17 shows a comparison among several speed observer in zero speed operation with the machine fully magnetized. Even in this case the TLS full order observer exhibits the best behaviour maintaining a stable working condition during the entire test.

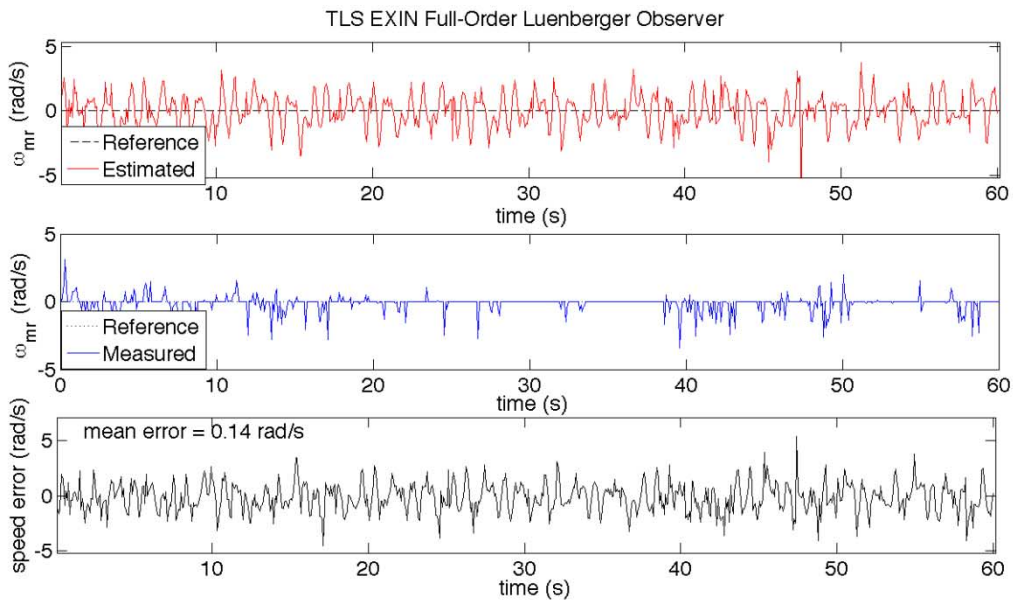


Fig. 14: reference, estimated, measured speed and speed estimation error during zero speed operation at no-load with the TLS EXIN Full-Order Luenberger Adaptive Observer

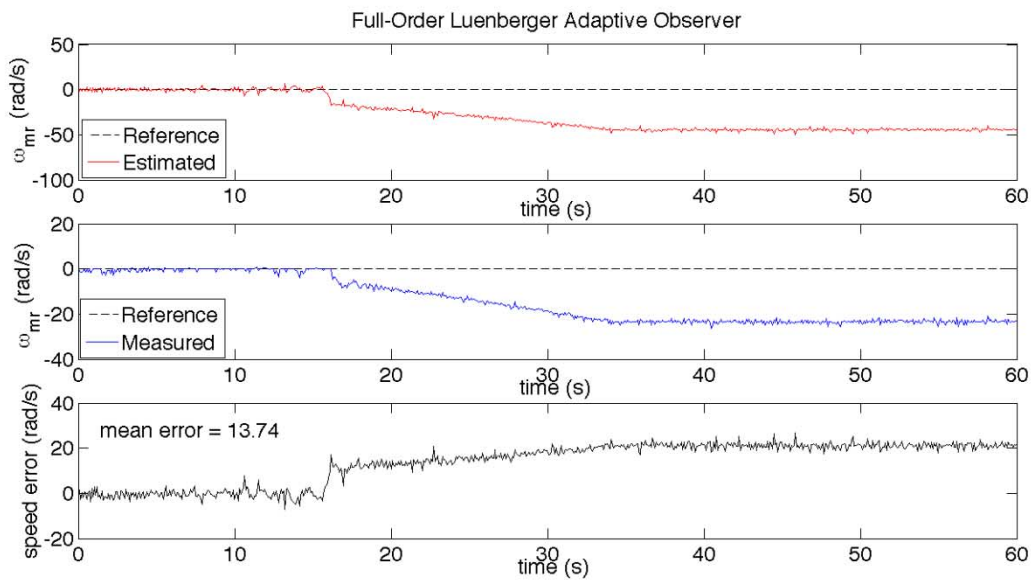


Fig. 15: reference, estimated, measured speed and speed estimation error during zero speed operation at no-load with the classical Full-Order Luenberger Adaptive Observer

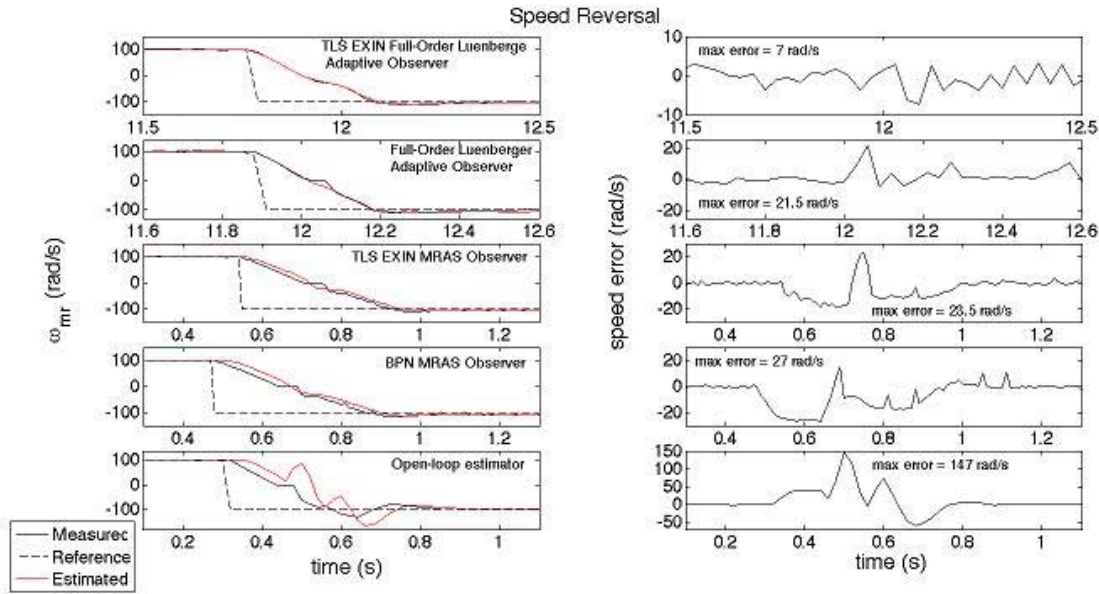


Fig. 16: Comparison among several speed observer in a speed reversal from 100 rad/s to -100 rad/s

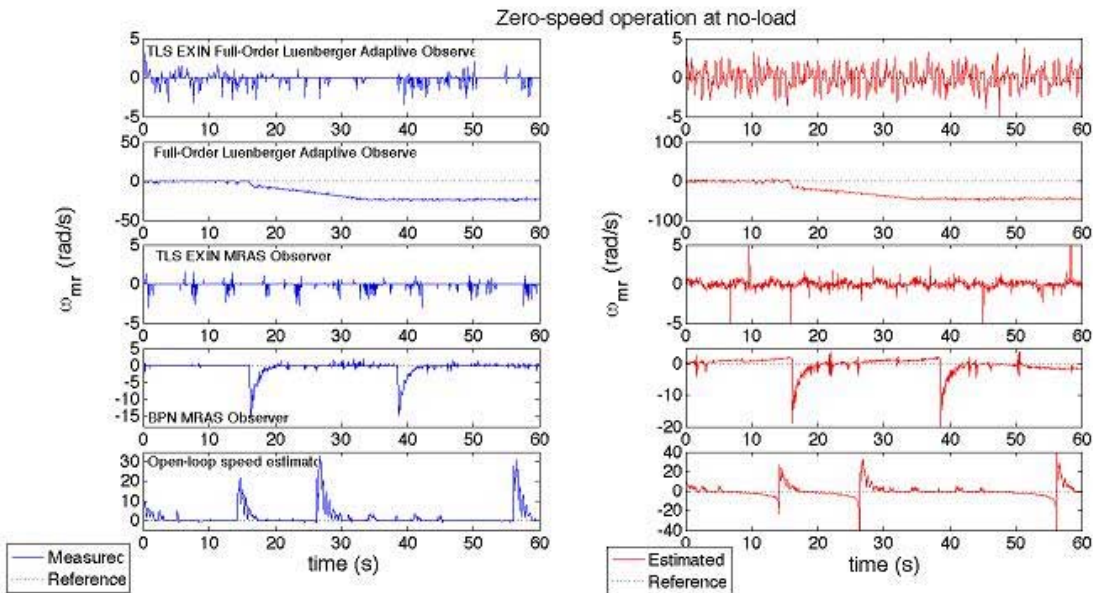


Fig. 17: Comparison among several speed observer with zero speed operation at no load

4.6 Conclusions

As a conclusion, apart from the possibility of the TLS EXIN full observer, some comparative results are shown obtained with other speed observers, summarized in Tab. III. with regard to the main issues of sensorless algorithms (score 1 corresponds to the best and 5 to the worst). It shows that the proposed TLS EXIN Full-Order Luenberger Adaptive Observer outperforms all the other observers in all the specified issues. The TLS MRAS Observer appears superior to the TLS MARS Observer [42], the Classic Adaptive Observer, the BPN MRAS Observer [35][36], and the open-loop estimator [9, § 6.4.5] in all issues, except for the accuracy in speed transient, where the Classic Adaptive Observer has a better behaviour. Remark that the Classic Adaptive Observer and BPN MRAS Observer are unable to deal with the regeneration mode at low speed and the field-weakening behaviour respectively.

Table III

Comparative results between speed observers (score 1 corresponds to the best and 5 to the worst).					
	Accuracy in Speed Transient	Minimum speed	Zero-speed operation	Field-weakening Behaviour	Regeneration mode at low speed
TLS MRAS Observer	3	2	2	1	1
TLS Adaptive Observer	1	1	1	1	1
Classic Adaptive Observer	2	3	5	1	NO
BPN MRAS Observer	4	5	3	NO	1
Open-loop estimator	5	4	4	1	1

5. Neural Enhanced Single-phase distributed generation systems with active power filtering capability.

This section deals with the use of linear neural network to improve the performance of a Distributed Generation (DG) system with Active Power Filtering (APF) capability. These two areas of power electronics make use of the most recent advances in control system technology. As shown in [9], the same power circuit topology can be utilized both for power inverter and for active filtering. Actually these functions can be performed by the same circuit if a suitable neural network based control is selected. In particular, the inverter functions are those of a DG unit that, connected in parallel with the grid, injects into the same grid a current with phase and frequency equal to the corresponding ones of the grid voltage and with amplitude depending on the power available from the renewable sources; on the other hand, the APF unit injects system harmonic currents like those of the loads but with opposite phase, thus keeping the line current almost sinusoidal. The task of the neural network consists of both the detection of the grid voltage fundamental and the computation of the load harmonic compensation current.

This section presents and discusses the results obtained experimentally on a 130 V rms, 50 Hz single-phase distribution network, which in itself contains the distorted currents coming from both the utility and a nonlinear load. The system described utilizes twice the same neural adaptive filter based on linear neurons (ADALINES): it is employed respectively to compute the fundamental component of the grid voltage waveform for the grid connection, and the overall harmonic component of the load current for the current harmonic compensation. In the first configuration the network allows the fundamental grid frequency voltage to be detected suppressing other components and is called “band” configuration; in the second all current harmonic components are detected and the fundamental is eliminated: it is called “notch” configuration. It should be noted that this approach does not need any a priori training of the neural network, which adapts itself on-line.

Fig. 18 shows the block diagram of the Neural Enhanced Single-phase DG systems with APF Capability; four main blocks are recognizable: the grid with its point of common coupling (PCC), the power unit that contains the inverter, the measurement units with all parameters to be acquired and finally the microprocessor units that includes the NN based filters.

The grid is modelled by a sinusoidal generator with series impedance and various linear and non-linear loads are connected to the PCC, which contains the inverter terminals connected to the power line and the current and voltage transducers. In particular the grid current i_g , the inverter current i , the load current i_L and the voltage v_{cp} are measured at the PCC.

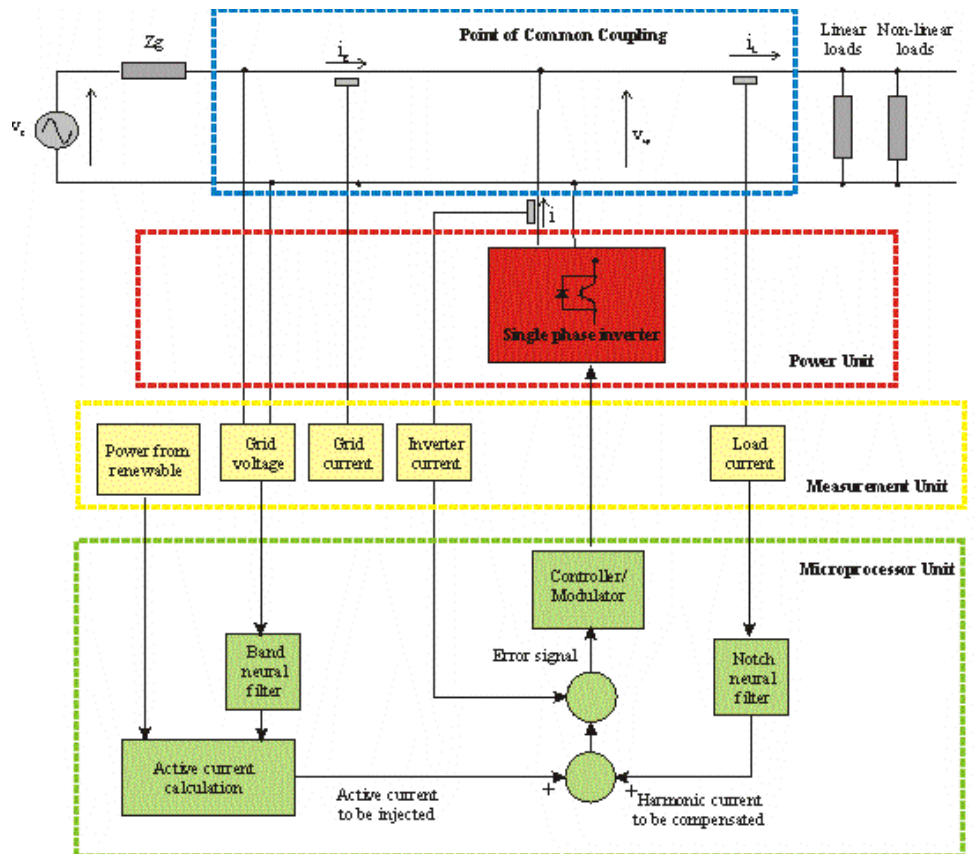


Fig.18: Block diagram of the Neural Enhanced Single-phase DG systems with APF Capability

The power unit contains the H-bridge inverter with its connecting inductance. The measurement unit contains all transducers to allow the main parameters to be converted into a suitable scaled voltage. Finally, the microprocessor unit receives information by the transducers, computes both the active current to be injected and the harmonic current to be compensated on the basis of NN based filters performance and outputs the signal to drive the inverter power devices.

5.1 Description of the Linear Neural Network

The neural network is represented in fig. 19.

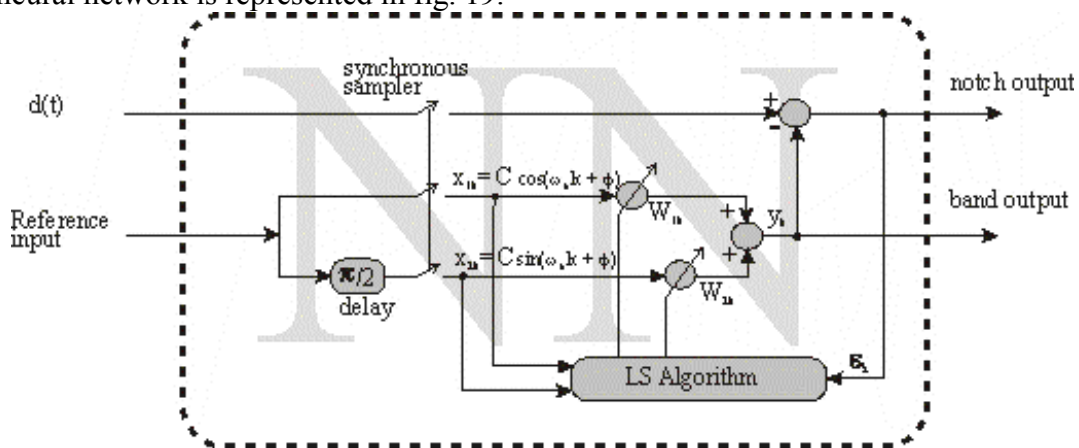


Fig. 19: Block diagram of the linear neural network

The network presents two inputs and two outputs. The first input is the signal to be processed; the second is a sinusoidal sequence with reference pulsation ω_0 . The two outputs give the notch and the band behaviour.

It should be noted that the neuron weights are adapted by the simple on-line training LMS algorithm by Widrow and Stearns [12] because of its low complexity, low computational demand and high speed convergence. Moreover this does not result in significant increase of the computational demand and complexity of the filters. The reference input is delayed by $\pi/2$ to build the 2nd sinusoidal reference and the frequency of these reference inputs corresponds to the frequency of the primary input signal d_k that should be cancelled or let pass, where k is the current sampled time instant.

Update of the weights, using the LMS, is given by:

$$\begin{cases} w_{1,k+1} = w_{1k} + 2\mu\varepsilon_k x_{1k} \\ w_{2,k+1} = w_{2k} + 2\mu\varepsilon_k x_{2k} \end{cases} \quad (24)$$

where w_{ik} is the weight of the i -th neuron at the k -th time sample, μ is the learning rate, and ε_k is the difference between the primary input signal d_k and the band filter output y_k ; ε_k is also the notch filter output. The sampled reference inputs are given by:

$$\begin{cases} x_{1k} = C \cos(k\omega_0 + \phi) \\ x_{2k} = C \sin(k\omega_0 + \phi) \end{cases} \quad (25)$$

where C is the amplitude of the sinusoidal sequence with reference frequency ω_0 .

The network transfer functions in z -domain has the following form:

$$\begin{cases} H(z) = \frac{z^2 - 2z \cos \omega_0 + 1}{z^2 - 2(1 - \mu C^2)z \cos \omega_0 + 1 - 2\mu C^2} & \text{notch filter} \\ K(z) = \frac{2\mu C^2(z \cos \omega_0 - 1)}{z^2 - 2(1 - \mu C^2)z \cos \omega_0 + 1 - 2\mu C^2} & \text{band filter} \end{cases} \quad (26)$$

The internal parameter μ has to be set to obtain a good trade off between the bandwidth and the convergence speed, this is crucial for the network to perform as a filter and for the overall stability of the system. As a matter of fact a slow convergence, corresponding to a lower value of μ and a narrower band introduces a delay that, in a feedback action could be unacceptable.

In particular the constraints for the harmonic voltage fundamental frequency extraction are: *the reference sequence pulsation* that has to be fixed to the rated value of the grid pulsation, *the bandwidth* that has to contain the slight variation permitted by standards to keep the filter working properly in presence of grid frequency variations. Anyway, the 2nd harmonic and interharmonics are suppressed because they lie outside the bandwidth of the filter. It is important to remark that filter stability considerations determine the upper limit of μ on the basis of the maximum eigenvalue of the autocorrelation matrix λ_{\max} then: $\frac{1}{\lambda_{\max}} > \mu > 0$. The optimal choice of μ is different for notch and band operation and is discussed in [9].

5.1.1 Notch operation

This output aims at suppressing a single frequency (or a very narrow band frequency) of the input signal. The frequency content outside the band of the filter remains unchanged both in amplitude and phase. This function is used to eliminate the fundamental current component and consequently to detect all current harmonic components.

If the stability of the filter is ensured, the following considerations for choosing the values of the parameter μ hold:

1. a narrow notch permits the compensation even of the load low frequency current harmonics; on the other hand, even if the grid frequency presents a slight shift respect to the nominal value, in the range allowed by standards, it has to be eliminated as well.

2. a narrow notch permits the filter to have a better phase characteristics around the notch frequency, with a phase characteristics equal to zero (zero delay time of the filter at all harmonics) at frequencies very close to the notch one. In this way there is no phase distortion of the load harmonic compensation current even at low frequency harmonics.

Fig. 20 shows the Bode diagram of the notch filter for different values of the parameter μ . It should be noted that constraints are satisfied for $\mu=8 \cdot 10^{-4}$ that gives a bandwidth equal to 2 Hz and exhibits a linear phase in the region where there are harmonics to be compensated. Two wrong choices are plotted too. It should be noted that for $\mu=1 \cdot 10^{-4}$ the bandwidth is too narrow and for $\mu=20 \cdot 10^{-4}$ the phase is different from zero in the range of current harmonics.

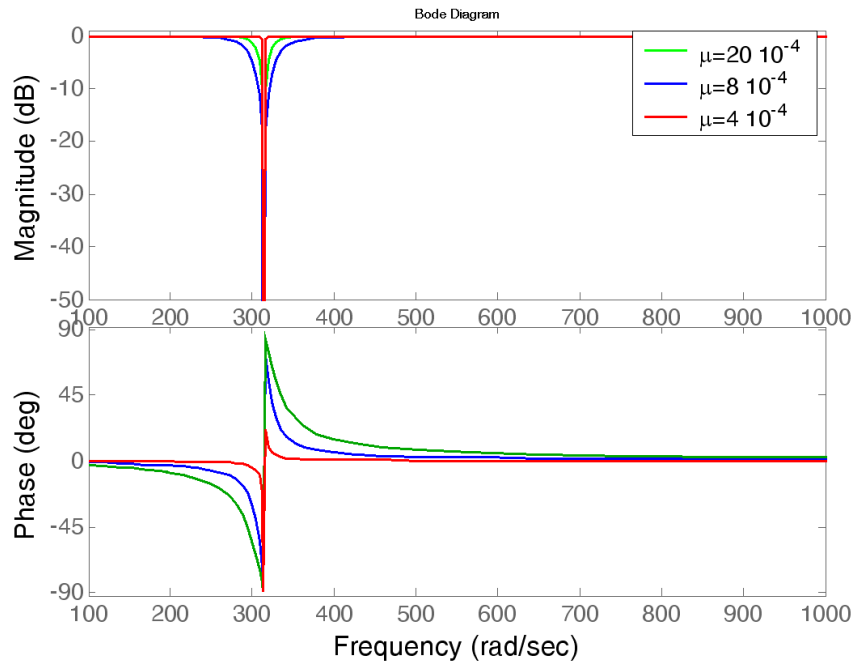


Fig. 20: Frequency response of the neural adaptive filter in notch configuration for different values of μ

5.1.2 Band operation

This function is used to detect the fundamental grid frequency voltage by suppressing other harmonics and interharmonics coming from the grid.

Taking into consideration, as example, the standard IEC61727 [43], the frequency range for normal grid operation is 50 ± 1 Hz. As a consequence the fundamental frequency is expected in the range from 49 Hz to 51 Hz.

With regard to the band neural filter μ can be chosen so as to have a slightly wider band than the grid fundamental frequencies allowed by standards, and this for two reasons:

1. a slightly wider band of the filter permits it to converge quickly, which is very important for a fast connection of the DG to the grid.
2. a slightly wider band of the filter permits the DG to connect properly to the grid even in presence of small variations of the grid frequency. With this regard, choosing a wider band permits the filter to have a better phase characteristics around the band frequency (close to zero), which is particularly important when the grid connection is to be done in presence of a modified grid frequency. In this way, a grid frequency tracking system is not strictly needed (see the PLL in [44]).

The plot of the Bode diagram is shown in Fig. 21. It should be noted that by adopting $\mu=20 \cdot 10^{-4}$ a bandwidth from about 43 Hz to 57 Hz is obtained. Moreover the Bode diagrams strongly decreases outside the filter bandwidth so as to erase other harmonics. As example it can be observed that the 3rd harmonic has attenuation greater than 20 dB.

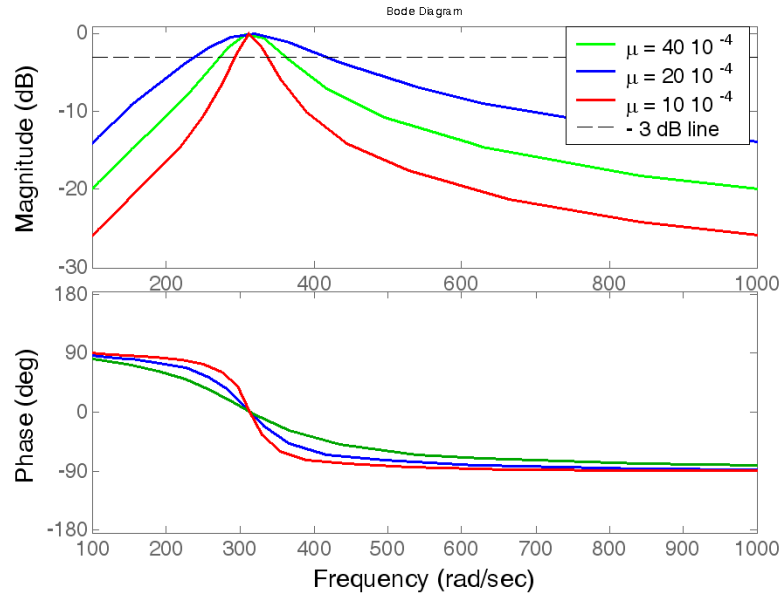


Fig. 21: Frequency response of the neural adaptive filter in band configuration for different values of μ

5.2 Building the current reference

The desired current to be supplied by the grid is sinusoidal, as a consequence all harmonics components different from fundamental one have to be suppressed and the reference i^*_{comp} will contain these terms with opposite phase. This function is performed by notch neural filter (see Fig. 20) that eliminates from the load current the fundamental current component.

On the basis of the power given by the renewable source P_{ref} , the active current reference is calculated and added to the reference to supply active power to the grid. This reference component i^*_{act} is obtained as (see Fig. 22b):

$$i^*_{act} = \frac{2P_{ref}}{v_{cpfilt}^2 + v'_{cpfilt}{}^2} v_{cpfilt} \quad (27)$$

where v_{cpfilt} is the output of the neural band adaptive filter, it contains only the grid voltage fundamental component. By a fictitious voltage, v'_{cpfilt} which is in quadrature with v_{cpfilt} , obtained shifting this last signal in time by a discrete time delay z^{-75} (75 samples at 15 kHz sampling frequency of the control system correspond to 5 ms, which is a quarter of period at 50 Hz). The denominator of eq. (27) is the square of the amplitude of the coupling point voltage. With such a scheme, the reference active current is generated to produce an amount of power equal to P_{ref} and is a sinusoid in steady-state, exactly in phase with the fundamental of the coupling point voltage v_{cp} : the DG therefore generates only active power with no reactive power exchanged with the grid. The availability of the grid harmonic voltage is crucial when a DG unit is connected close to a non-linear current load. As a matter of fact, the coupling point voltage v_{cp} can be influenced by the voltage drop on the grid impedance of the load current i_L becoming distorted too, moreover the DG can inject current harmonics into the same grid impedance worsening the shape of grid voltage shape.

5.3 Experimental results

The single-phase sinusoidal electrical grid at 130 V rms, 50 Hz, sketched in Fig. 22a with parameters in tab. IV, has been considered for the experimental assessment of the method.

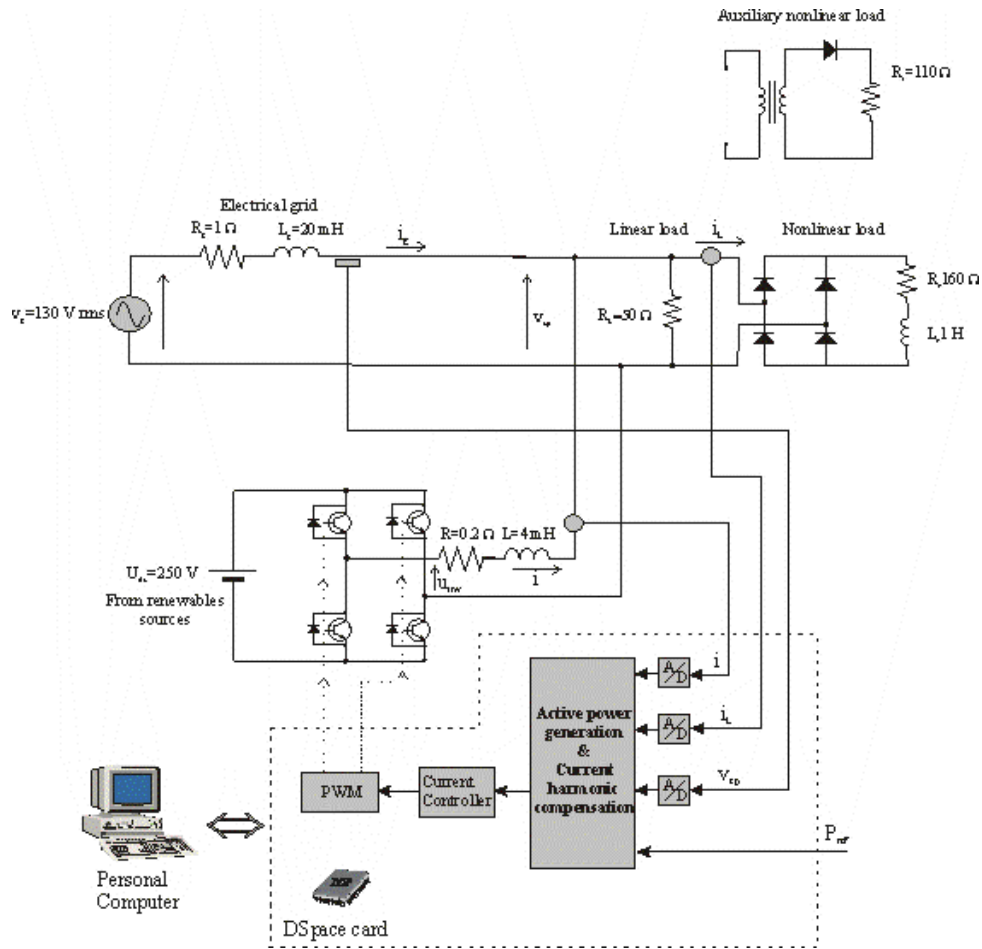


Fig: 22a: Electrical scheme of the DG unit with APF (Active Power Filtering)

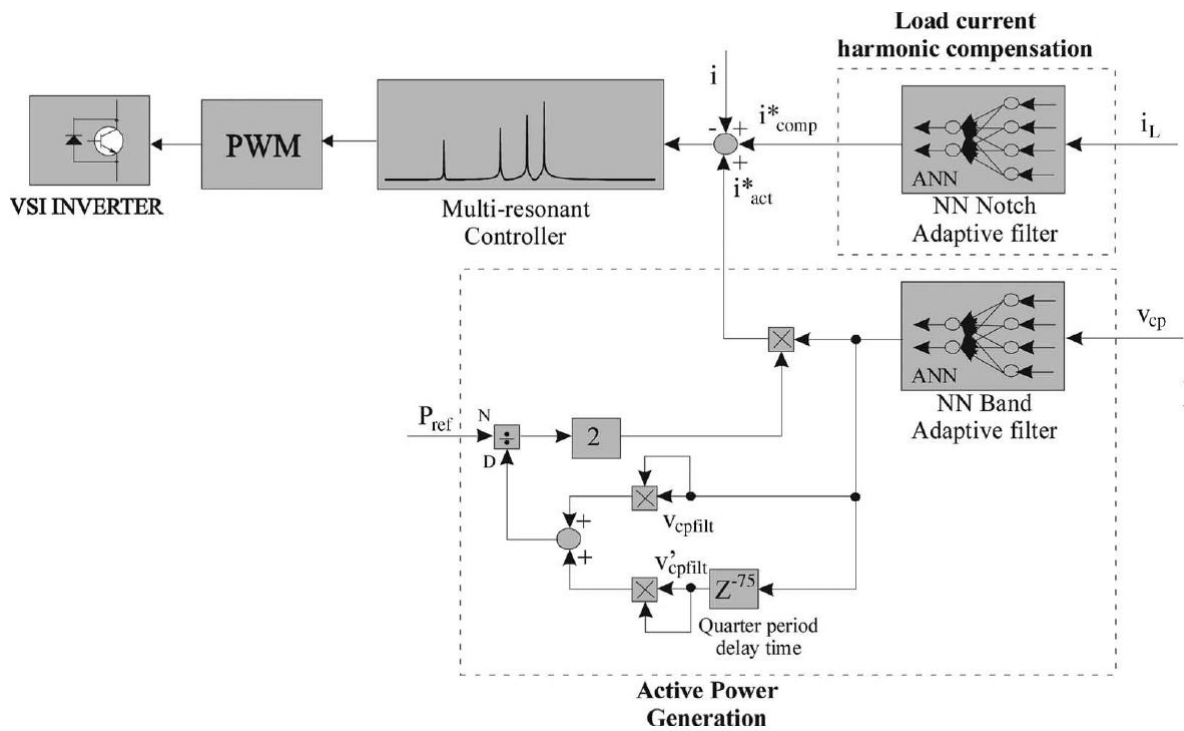


Fig: 22b: Block diagram of the DG/APF operation

Table IV:

Parameters of the grid		
L_g [mH]	= grid inductance	20
R_g [Ω]	= grid resistance	1
L [mH]	= interconnecting filter inductance	4
R [Ω]	= interconnecting filter resistance	0.2
V_g rms [V]	= grid voltage	130
U_d [V]	= DC voltage	250

The non-linear current load is obtained with a diode bridge supplying a highly inductive load, so the required current is almost a square wave. In addition an auxiliary non-linear load can be connected as an alternative to the previous one. This auxiliary load is obtained with a saturable transformer supplying a diode in series with a resistance load. The current waveform required by it is a complex waveform with both odd and even harmonics.

The single-phase inverter is connected to the grid by a filtering inductance, which smoothes the inverter current waveform. The inverter employs four IGBT modules type Semikron SMK 50 GB 123 in a H-bridge connection with their proper drivers. Three current sensors, model LEM LA 55-P, are used to measure respectively the grid, the inverter and the load current. A voltage sensor model LEM CV3-1000 has been used to measure the common coupling point (CCP) voltage. A sampling frequency of 15 kHz has been adopted both for the simulation and the experimental tests.

A renewable source (photovoltaic, wind, fuel-cells etc.) supplies with a dc voltage of $U_{dc}=250$ V a single-phase inverter. It is connected to the grid by a filtering inductance L (with parasitic resistance R). The DG-APF needs, to properly work, the acquisition of the inverter current i , the load current i_L and the voltage of the coupling point v_{cp} . These signals are acquired by a programmable hardware, a DSP in the case under study, in which are implemented both the load current harmonic compensation and the grid connection features.

Fig. 23 shows the block diagram of the whole system. Remark the use of a resonant converter tuned at the grid frequency and at the 3rd, 5th and 7th harmonics. The controller tuned at the fundamental frequency is used for the active power generation, while the three resonant harmonic controllers are used either for the load current compensation (APF capability ON) or to control to zero the first three odd harmonics of the injected current (APF capability OFF).

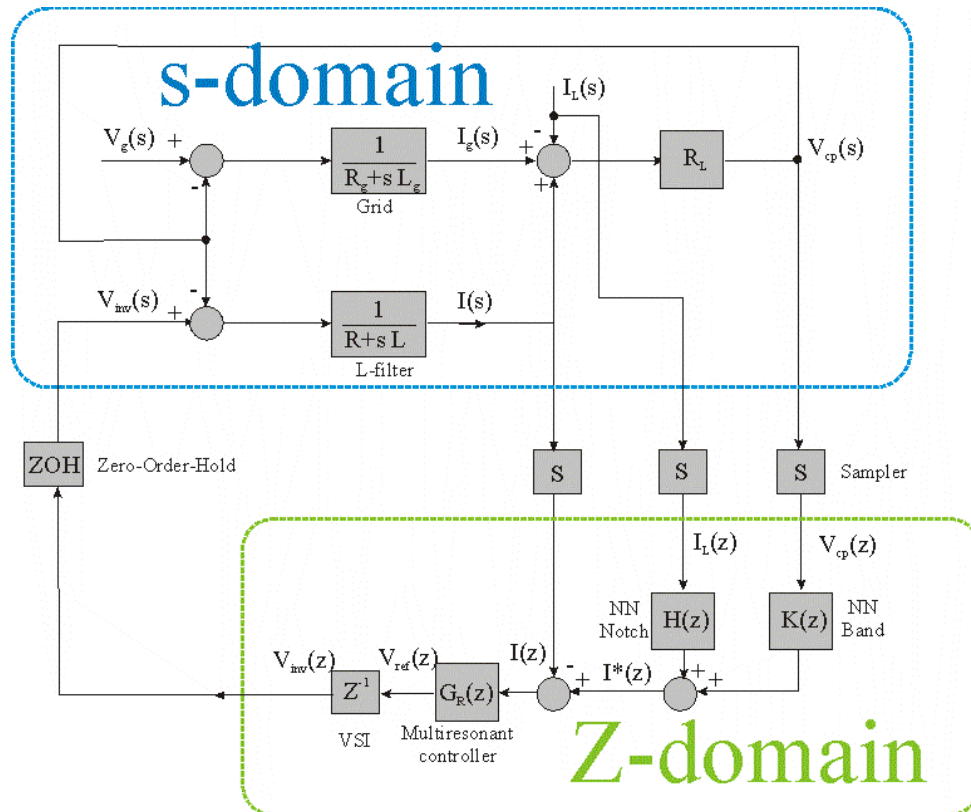


Fig.23: Block diagram of the DG unit

Fig. 24 shows on the left the steady-state time waveform of the current required by the non-linear current load and its harmonic content obtained with the FFT (Fast Fourier Transform). It is a quasi-square waveform, presenting only odd harmonics with amplitude decreasing with inverse proportionality with the frequency, whose %THD (Total Harmonic Distortion) computed up to the 19th harmonics is 25.2%. On the right side of Fig. 10.17 there is the steady-state time waveform of the current required by the auxiliary non-linear current load and its harmonic content: here also even harmonics are present and the corresponding %THD is equal to 43%.

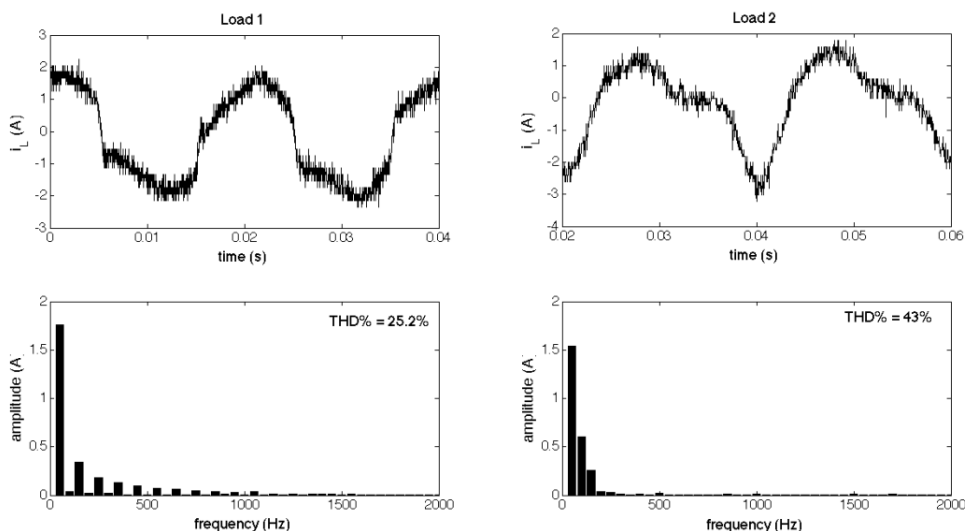


Fig. 24: measured current waveform required by the nonlinear load and its spectrum (left) and by the auxiliary non-linear load (right)

Two kinds of challenging tests have been studied in the proposed system. The first consists in the sudden insertion of the active filtering capability (APF) keeping a active power reference equal to zero. It corresponds to the operation of a pure shunt power APF. Then a second step reference of active power of 600 W is given, when the DG is already working in active filtering mode, reproducing the case when additional power is available from the renewable source. In this last case the generation of active power to supply the grid is required in addition to APF performance.

5.3.1 APF insertion

Fig. 25 shows the effects of the sudden insertion of the APF on the grid, with null active power reference, obtained experimentally with the DG-APF based on Neural Adaptive Filtering. The APF is operated at $t=0$, before this time the grid current is equal to that required by the non-linear load. In particular, Fig. 25 shows the inverter current waveforms (reference and measured), the load and grid current and finally the coupling point voltage (measured and filtered by the NN band filter) and its fictitious quadrature component and the reference voltage provided to the PWM modulator. In this test the linear resistance is not connected. It can be observed that, after the APF insertion, the inverter current rapidly gets the reference one (in few cycles of the fundamental), while the load grid current, initially equal to the nonlinear load one, becomes close to a sinusoid. At the same time the coupling point voltage becomes slightly noisier after the APF insertion, as expected, due to the injected current by the inverter, and the NN filter $K(z)$ correctly extracts the fundamental harmonics of the grid voltage, as it works in band mode. Fig. 26 shows the steady-state waveform of the inverter current and its spectrum, obtained with the FFT, at the end of the transient in Fig. 25. In APF mode the inverter generates a current with a harmonic content which presents a high 3rd harmonic of the grid fundamental (see the harmonic content of the nonlinear load of fig. 24), controlled by the corresponding resonant controller, as well as some undesired multiples of it. Correspondingly fig. 27 shows the steady-state grid current and its spectrum, which, after the insertion of the APF, is basically a sinusoid: the 3rd, 5th and 7th harmonics are correctly eliminated by the multiresonant controller driven by the neural notch filter $H(z)$ and the first meaningful harmonic is the 9th, which, even if not controlled, has an amplitude which is less than 4% of the fundamental. The total %THD of the grid current is 4.51%.

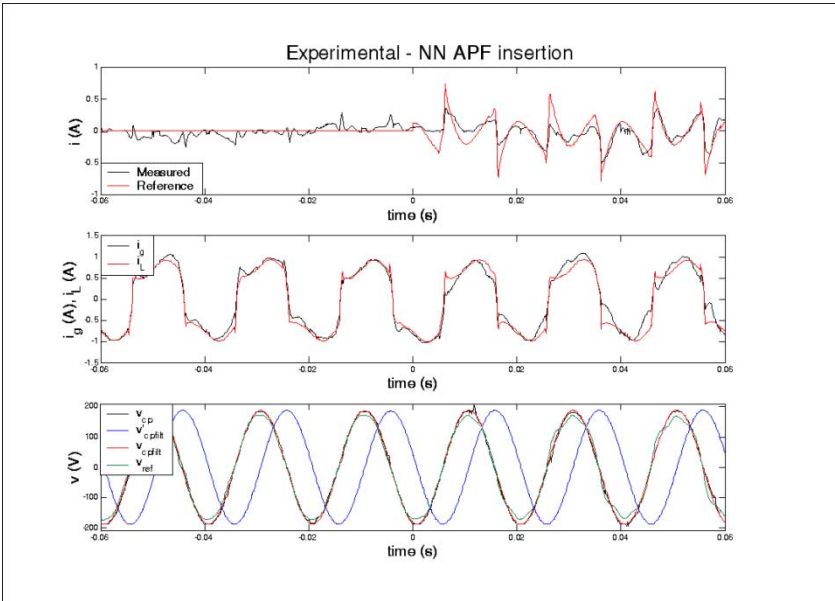


Fig. 25: measured grid current, inverter current, load current and coupling point voltage during the transient of the insertion of APF with the DG-APF based on Neural Adaptive Filtering.

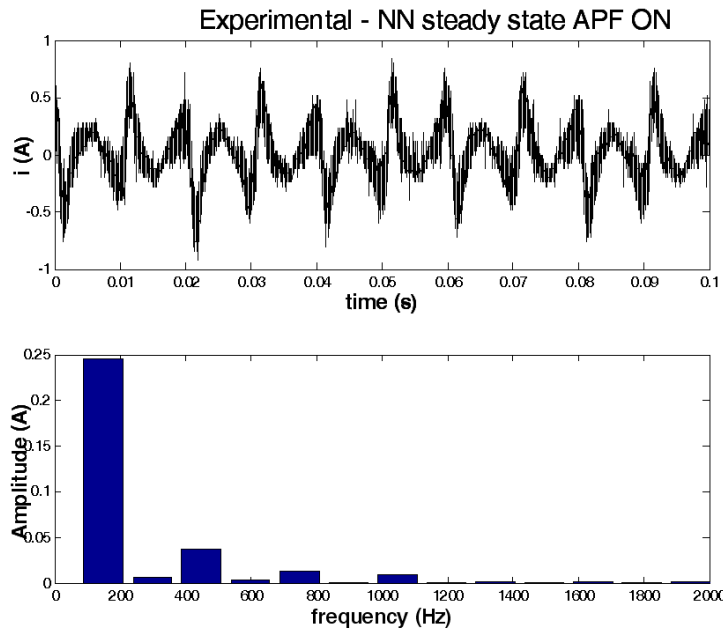


Fig. 26: measured steady-state of the inverter current with APF ON with the DG-APF based on Neural Adaptive Filtering

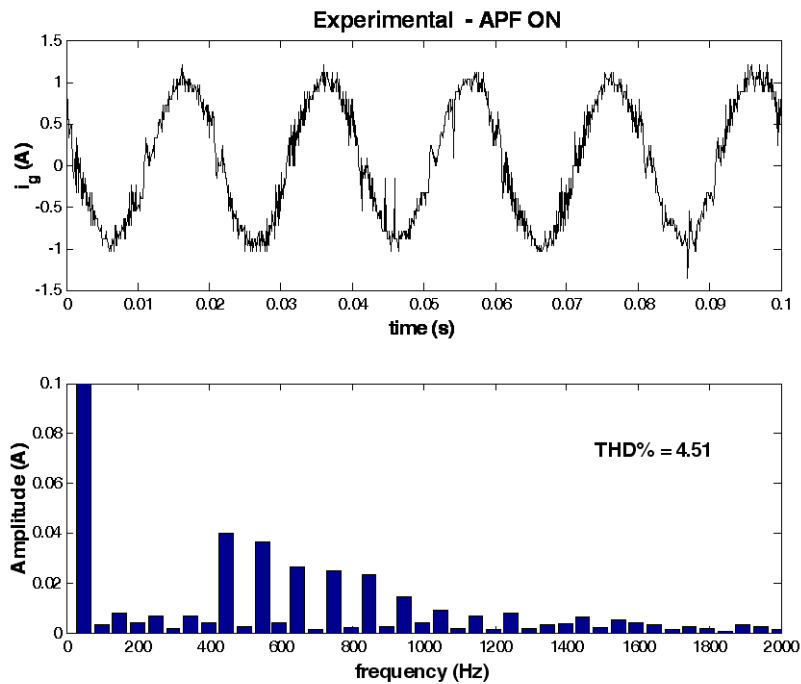


Fig. 27: measured steady-state grid current with APF on with the DG-APF based on Neural Adaptive Filtering

5.3.2 Power reference insertion

In this test, during the APF operation, a step power reference is given as when energy is suddenly available from a renewable source. A step of 600 W has been chosen. Both linear (R_L) and non linear loads are connected to the grid.

The effects of this step power reference, given at $t=0$, are shown in Fig. 28. Particularly, the following parameters are included: the inverter current waveforms (reference and measured), the load and grid current and finally the coupling point voltage (measured and filtered by the NN band filter) and its fictitious quadrature component, and finally the reference voltage provided to the PWM modulator. The top diagram contains the measured current (i), the reference active current due to power step (i_{act}^*), the reference current due to the APF operation (i_{comp}^*) comprising the outputs of $H(z)$ and $K(z)$, and the sum of the last two terms ($i^* = i_{act}^* + i_{comp}^*$). After the power step, the active current reference component rises and is in phase with the filtered coupling point voltage thanks to the operation of NN band filter $K(z)$. The inverter current rapidly converges to the reference one in about three cycles of the grid fundamental and without any overshoot.

The middle diagram contains the grid current (i_g), the load current (i_L) and again the inverter current (i). After the power step, the grid current changes its sign because the amount of power generated by the DG is higher than the sum of the power required both by the linear and nonlinear loads. The inverter and grid currents present correspondingly in steady-state opposite signs.

Finally, the bottom diagram shows the voltage and, particularly, the voltage in the point of common coupling (V_{cp}), the corresponding filtered one (V_{cpfilt}) and delayed of $\pi/4$ (V'_{cpfilt}) and the reference voltage (V_{ref}). The reference voltage provided to the PWM modulator is lower than the coupling point voltage before the power step and then, when it operates as DG, it becomes higher.

Fig. 29 shows the steady-state time waveform of the inverter current and its spectrum obtained with the FFT at the end of the transient in fig.28. The aim of this picture is to show that the inverter current is basically a sinusoid at 50 Hz, apart from the 3rd, 5th and 7th harmonics which are exactly equal to the corresponding harmonic components of the load current (before APF operation the load current was practically the one shown in Fig. 24) but now they are generated by the inverter because the APF capability is on. If the APF capability were set off, the multiresonant controller would have zero references of these harmonics, which would therefore be actively controlled to zero. The resulting %THD is equal to 4.74%.

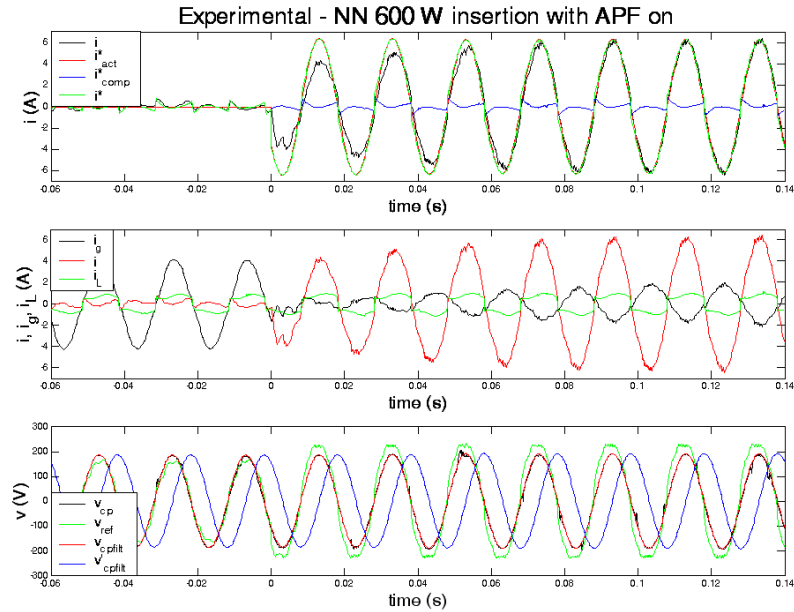


Fig. 28: grid current, inverter current, load current and coupling point voltage during the step transient of Pref=600 W with APF on with the DG-APF based on Neural Adaptive Filtering (experiment).

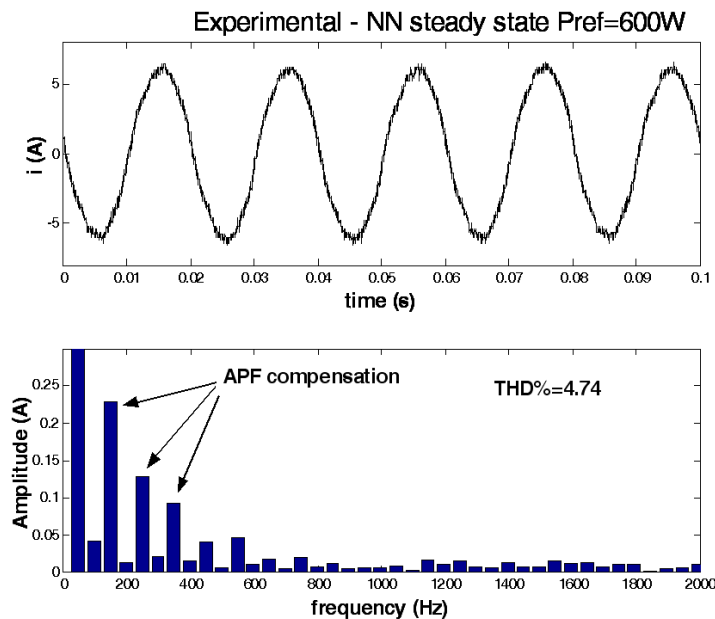


Fig. 29: steady-state inverter current with Pref=600 W with APF on with the DG-APF based on Neural Adaptive Filtering (experiment)

6. Conclusions

This paper gives only a brief description of the possible capabilities of linear neuron networks to power electronics applications, spanning from parameter identification of electrical machines to power quality and active filtering and finally to sensorless control for high performance electrical drives. These techniques, thanks to their simplicity, have made it possible a bunch of applications. At present other applications to linear control and identification of linear induction motors and to PMSM sensorless control are under investigation. The main point to stress here is that these neurons have a solid analytical

background, thanks to which the TLS techniques have been employed: the use of Total Least Squares is much more suitable for real world scenarios, since data are always affected by noise. Moreover the use of linear neurons as easy to implement adaptive filters has proved to be most useful for power quality and active filtering in multisource systems connected to the grid in a plug-and-play fashion. Theoretical background and experimental results show how these techniques are now mature enough for several applications.

List of symbols

- u_{sA}, u_{sB}, u_{sC} = stator phase voltages;
 i_{sA}, i_{sB}, i_{sC} = stator phase currents;
 $\mathbf{u}_s = u_{sD} + j u_{sQ}$ = space-vector of the stator voltages in the stator reference frame;
 $\mathbf{u}_s^g = u_{sx}^g + j u_{sy}^g$ = space-vector of the stator voltages in a generic rotating reference frame;
 $\mathbf{i}_s = i_{sD} + j i_{sQ}$ = space-vector of the stator currents in the stator reference frame;
 $\mathbf{i}_s^g = i_{sx}^g + j i_{sy}^g$ = space-vector of the stator currents in a generic rotating reference frame;
 $\mathbf{i}_r = i_{rd} + j i_{rq}$ = space-vector of the rotor currents in the stator reference frame;
 $\mathbf{i}_r^g = i_{rx}^g + j i_{ry}^g$ = space-vector of the rotor currents in a generic rotating reference frame;
 $\Psi_r = \Psi_{rd} + j \Psi_{rq}$ = space-vector of the rotor flux-linkages in the stator reference frame;
 $\Psi_s = \Psi_{sD} + j \Psi_{sQ}$ = space-vector of the stator flux-linkages in the stator reference frame;
 $\mathbf{i}_{mr} = i_{mrD} + j i_{mrQ}$ = space-vector of the rotor magnetizing current in the stator reference frame;
 $\mathbf{i}_{ms} = i_{msD} + j i_{msQ}$ = space-vector of the stator magnetizing current in the stator reference frame;
 $\mathbf{i}_{mm} = i_{mmD} + j i_{mmQ}$ = space-vector of the magnetizing current in the stator reference frame;
 ρ_r = phase angle of the rotor flux linkage space vector with respect to the sD axis;
 ρ_s = phase angle of the stator flux linkage space vector with respect to the sD axis;
 ρ_m = phase angle of the magnetizing flux linkage space vector with respect to the sD axis;
 ϑ_r = angular position of the rotor with respect to the sD axis;
 L_s = stator inductance;
 L_s' = stator transient inductance;
 L_r = rotor inductance.
 L_m = total static magnetising inductance;
 $L_{s\sigma}$ = stator leakage inductance;
 $L_{r\sigma}$ = rotor leakage inductance;
 R_s = resistance of a stator phase winding;
 R_r = resistance of a rotor phase winding;
 T_s = stator time constant;
 T_r = rotor time constant;
 $\beta_0 = R_r/L_r$ = inverse of the rotor time constant T_r ;
 T_s' = stator transient time constant;
 T_r' = rotor transient time constant;
 $T_{r\sigma}$ = rotor leakage time constant;
 $\sigma = 1 - L_m^2/(L_s L_r)$ = total leakage factor;
 σ_r = rotor leakage factor;

σ_s = stator leakage factor;
 p = number of pole pairs;
 ω_{mr} = angular speed of the rotor flux space-vector;
 ω_{ms} = angular speed of the stator flux space-vector;
 ω_{mm} = angular speed of the magnetizing flux space-vector;
 ω_{sl} = angular slip speed;
 ω_r = angular rotor speed (in electrical angles per second);
 t_e = electromagnetic torque;

References

- [1] P. Vas, "Sensorless Vector and Direct Torque Control", Oxford Science Publication, 1998.
- [2] P. Vas, Artificial-Intelligence-Based Electrical Machines and Drives, Oxford Science Publications, 1999.
- [3] P. Vas, W. Drury, A F Stronach, "Recent Developments in Artificial Intelligence Based Drives – A Review". PCIM, Nürnberg, 299-315, 1996.
- [4] B.K Bose, "Fuzzy logic and neural networks in power electronics and drives", IEEE Ind. Appl. Mag., vol. 6 , n. 3, 2000 , pp. 57 – 63.
- [5] B.K Bose, "Power electronics-an emerging technology", IEEE Trans. on Ind. Electr., vol. 36 , n. 3, 1989, pp. 403 – 412.
- [6] B.K Bose, "Expert system, fuzzy logic, and neural network applications in power electronics and motion control", Proceedings of the IEEE, vol. 82, n. 8, 1994, pp. 1303 – 1323.
- [7] B.K Bose, "Neural Network Applications in Power Electronics and Motor Drives—An Introduction and Perspective". IEEE Trans. on Ind. Electr., vol. 54 , n. 1, 2007 , pp. 14 – 33.
- [8] B.K Bose, "Power Electronics And Motor Drives: Advances and Trends", Academic Press September 2006, pp.936
- [9] M. Cirrincione, M.Pucci; G Vitale "Power Converters and AC Electrical Drives with Linear Neural Networks", p. 661, Boca Raton:CRC Press, Taylor & Francis Group, ISBN: 9781439818145, April 2012
- [10] S.K. Mondal, J.O.P. Pinto, B.K. Bose, "A neural-network-based space-vector PWM controller for a three-level voltage-fed inverter induction motor drive", IEEE Trans. on Ind. Appl., vol. 38 , n. 3, 2002 , pp. 660 – 669.
- [11] J.O.P. Pinto, B.K. Bose, L.E.B. Da Silva, M.P. Kazmierkowski, "A neural-network-based space-vector PWM controller for voltage-fed inverter induction motor drive", IEEE Trans. on Ind. Appl., vol. 36 , n.: 6 , 2000 , pp. 1628 – 1636.
- [12] B. Widrow, S. D. Stearns, "Adaptive Signal Processing", Prentice Hall, 1985
- [13] G.Cirrincione, M. Cirrincione, "Neural Based Orthogonal Data Fitting: The EXIN Neural Networks", Hoboken, New Jersey, John Wiley & Sons, Inc., , series : Adaptive and Learning Systems for Signal Processing, Communications and Control, 255 pages, November 2010, pp 277
- [14] S.D. Hodges and P.G. Moore. Data uncertainties and least square regression, *Applied Statistics*, (21) :185–195, 1972.
- [15] G.W. Stewart. Sensitivity coefficients for the effects of errors in the independent variables in a line regression. Technical Report TR-571, Department of Computer Science, University of Maryland, College Park, MD, 1977.
- [16] G.H. Golub and C.F. Van Loan. An analysis of the total least squares problem. *SIAM Journal of Numerical Analysis*, pages 883–893, 1980.
- [17] [8.38] P. Huber. *Robust Statistics*. Wiley, New York, 1981
- [18] R.D. Degroat and E. Dowling. The data least squares problem and channel equalization. *IEEE Trans. on Signal Processing*, 41(1) :407–411, January 1993
- [19] G.H. Golub and C. Reinsch. Singular value decomposition and least squares solutions. *Num. Math.*, (14) :403–420, 1970
- [20] S. Van Huffel and J. Vandewalle. *The Total Least Squares Problems : Computational Aspects and Analysis. Frontiers in Applied Mathematics*. SIAM Philadelphia, 1991.
- [21] M.F. Moller. A scaled conjugate gradient algorithm for fast supervised learning. *Neural Networks*, 6 :525–533, 1993.
- [22] W.H. Press, S.A. Teukolsky, W.T. Wetterling, and B.P. Flannery. *Numerical Recipes in C : The Art of Scientific Computing*. Cambridge University Press, second edition, 1992.
- [23] G. Cirrincione. *A Neural Approach to the Structure from Motion Problem*. PhD thesis, LIS INPG Grenoble, December 1998
- [24] W. Leonhard, Control of Electrical Drives, Springer-Verlag, 1997.
- [25] P. Vas, Sensorless Vector and Direct Torque Control, Oxford Science Publications, 1998

- [26] Hendrik Klaassen, *Selbsteinstellende, Feldorientierte Regelung einer Asynchronmaschine und geberlose Drehzahlregelung*, Dissertation, TU Braunschweig, 1999.
- [27] Nguyen Phung Quang, Jorg-Andreas Dittrich, *Praxis der feldorientierten Drehstrom-Antriebsregelungen*, Expert Verlag, 1999.
- [28] J. Stephan, M. Bodson, “Real-time estimation of the parameters and fluxes of induction motors”, *IEEE Trans. on Ind. Appl.*, vol. 30; n° 3, May/June 1994
- [29] M. Cirrincione , M. Pucci , G. Cirrincione , G. A. Capolino, “A New Experimental Application of Least-Squares Techniques for the Estimation of the Induction Motor Parameters ”, *IEEE Trans. on Ind. Appl.* vol. 39, n. 5, September/October 2003, pp. 1247-1256.
- [30] M. Cirrincione, M. Pucci, G. Cirrincione, G. Capolino, “Constrained Minimization for Parameter Estimation of Induction Motors in Saturated and Unsaturated Conditions ”, *IEEE Trans. on Ind. Electr.*, vol. 52, n. 5, October 2005
- [31] B. Karanayil, M. F. Rahman, C. Grantham, “Online Stator and Rotor Resistance Estimation Scheme Using Artificial Neural Networks for Vector Controlled Speed Sensorless Induction Motor Drive”, *IEEE Trans. on Ind. Electr.*, vol. 54 , n. 1, 2007 , pp. 167 – 176.
- [32] S.M. Gadoue, D. Giaouris, J.W. Finch, “Sensorless Control of Induction Motor Drives at Very Low and Zero Speeds Using Neural Network Flux Observers”, *IEEE Trans. on Ind. Electr.*, vol. 56, n. 8, 2009 , pp. 3029 – 3039.
- [33] M. Wlas, Z. Krzeminski, J. Guzinski, H. Abu-Rub, H.A. Toliyat, “Artificial-Neural-Network-Based Sensorless Nonlinear Control of Induction Motors”, *IEEE Trans. on Ener. Conv.*, vol. 20, n. 3, 2005 , pp. 520 – 528.
- [34] L. Ben-Brahim, R. Kurosawa, “Identification of Induction Motor Speed using Neural Networks”, *IEEE PCC*, 1993.
- [35] M. Elloumi, L. Ben-Brahim, M. Al-Hamadi, “Survey of Speed Sensorless Controls for IM drives”, *IEEE IECON*, 1998.
- [36] L. Ben-Brahim, “Motor speed identification via neural networks”, *IEEE Ind. Appl. Mag.*, vol. 1 , n. 1, 1995, pp. 28 – 32.
- [37] L. Ben-Brahim, S. Tadakuma, A. Akdag, “Speed Control of Induction Motor without Rotational Transducers”, *IEEE Trans. on Ind. Appl.*, vol. 35, n°4, pp. 844-850, July/August 1999.
- [38] T. Orłowska-Kowalska, M. Dybkowski, K. Szabat, “Adaptive Sliding-Mode Neuro-Fuzzy Control of the Two-Mass Induction Motor Drive Without Mechanical Sensors”. *IEEE Trans. on Ind. Electr.*, vol. 57, n. 2, 2010, pp. 553 – 564.
- [39] J.R. Heredia, F. Perez Hidalgo, J.L. Duran Paz, “Sensorless control of induction motors by artificial neural networks”, *IEEE Trans. on Ind. Electr.*, vol. 48 , n. 5, 2001, pp. 1038 – 1040
- [40] M. Cirrincione, M. Pucci, G. Cirrincione, G. Capolino, “Sensorless Control of Induction Machines by a New Neural Algorithm: the TLS EXIN Neuron”, *IEEE Trans. on Ind. Electr.*, vol. 54, n. 1, February 2007, Special Section Neural Network Applications in Power Electronics and Motor Drives (Guest Editor B.K. Bose).
- [41] M. Cirrincione, M. Pucci, G. Cirrincione, G. Capolino, “An Adaptive Speed Observer Based on a New Total Least-Squares Neuron for Induction Machine Drives”, *IEEE Trans. on Ind. Appl.*, vol. 42, n.1, January/February 2006, pp.89-104.
- [42] M. Cirrincione, M. Pucci, “ An MRAS Speed Sensorless High Performance Induction Motor Drive with a Predictive Adaptive Model “, *IEEE Trans. on Ind. Electr.*, vol.52, n. 2, April 2005.
- [43] IEEE standard 1547-2003 “IEEE Standard for interconnecting distributed resources with electric power systems”, Institute of Electrical and Electronics Engineering, New York, 2003.
- [44] Ciobotaru, R. Teodorescu, F. Blaabjerg, “A New Single-Phase PLL Structure Based on Second Order Generalized Integrator”, *Power Electronics Specialists Conference, 2006. PESC '06. 37th IEEE*, 18-22 June 2006, pp. 1 – 6